Performance Analysis and Evaluation of Photonic Waveguides for Multiprocessor Communications

A thesis submitted in partial fulfillment of the requirements for the award of degree of

Master of Technology

in

VLSI Design & CAD

Submitted By:

Hem Pushp Mittal

Roll No. 600961008

Under the Guidance of

Dr. Sanjay Sharma

Associate Professor

Department of Electronics & Communication Engineering

Thapar University, Patiala

June 2011

CERTIFICATE

I hereby declare that the work which is being presented in the thesis entitled"**Performance Analysis and Evaluation of Photonic Waveguides for Multiprocessor Communications**" in partial fulfillment of the requirement for the award of degree of M.Tech. (VLSI Design & CAD) at Electronics and Communication Engineering Department of Thapar University, Patiala, is an authentic record of my own work carried out under the supervision of Dr. Sanjay Sharma, Associate Professor, ECED.

The matter presented in this thesis has not been submitted in any other University/Institute for the award of my degree.

Date: 30 June 2011

Hem Pushp Mittal
Roll.No.600961008

It is certified that the above statement made by the student is correct to the best of my knowledge and belief.

30/6/2011

Dr. Sanjay Sharma
Associate Professor
ECED,Thapar University

Counter signed by:

Dr. A. K. Chatterjee
Professor & Head
ECED, Thapar University
Patiala-147004

Dr. S. K. Mahopatra
Dean of Academic Affairs
Thapar University
Patiala-147004

[I]

ACKNOWLEDGEMENTS

I take this opportunity to express my profound sense of gratitude and respect to all those who helped me through the duration of this thesis. I would have never succeeded in completing my task without the cooperation, encouragement and help provided to me by various people. Words are often too less to reveals one's deep regards. I acknowledge with gratitude and humility my indebtedness to **Dr. Sanjay Sharma, Associate Professor,** Electronics and Communication Engineering Department, Thapar University, Patiala, under whose guidance I had the privilege to complete this thesis. I wish to express my deep gratitude towards him for providing individual guidance and support throughout the thesis work.

I convey my sincere thanks to **HEAD OF THE DEPARTMENT, Dr. A. K. Chatterjee** as well as **PG Coordinator, Dr. Alpana Agrawal, Assistant Professor,** Electronics and Communication Engineering Department, entire faculty and staff of Electronics and Communication Engineering Department for their encouragement and cooperation.

I would also like to thank my friends who were always there at the need of the hour and provided me all the help and facilities, which I required for the completion of my thesis.

My greatest thanks are to all who wished me success especially my parents. Above all I render my gratitude to the Almighty who bestowed self-confidence, ability and strength in me to complete this work for not letting me down at the time of crisis and showing me the silver lining in the dark clouds. I do not find enough words with which I can express my feelings of thanks to my dear friends for their help, inspiration and moral support which went a long way in successful competition of the present study.

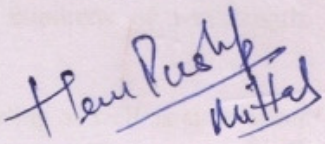

Hem Pushp Mittal

ABSTRACT

After dominating the electronics industry for decades, silicon is on the verge of becoming the material of choice for the photonics industry: the traditional stronghold of III–V semiconductors. Stimulated by a series of recent breakthroughs and propelled by increasing investments by governments and the private sector, silicon photonics is now the most active discipline within the field of integrated optics. This paper provides an overview of the state of the art in silicon photonics and outlines challenges that must be overcome before large-scale commercialization can occur. In particular, for realization of integration with CMOS very large scale integration (VLSI), silicon photonics must be compatible with the economics of silicon manufacturing and must operate within thermal constraints of VLSI chips. The impact of silicon photonics will reach beyond optical communication—its traditionally anticipated application. Silicon has excellent linear and nonlinear optical properties in the midwave infrared (IR) spectrum. These properties, along with silicon's excellent thermal conductivity and optical damage threshold, open up the possibility for a new class of mid-IR photonic devices.

Photonic band gap (PBG) materials are periodic dielectric structures that forbid propagation of electromagnetic waves in a certain frequency range. They are able to engineer the most fundamental properties of electromagnetic waves, such as the laws of refraction, diffraction and emission of light from atoms. Such PBG materials not only open up a variety of possible applications, but also give rise to new physics. Unlike electronic micro-cavity, optical waveguides in a PBG microchip can simultaneously conduct hundreds of wavelength channels of information in a three-dimensional circuit path.

The thesis starts with the numerical modeling techniques for modeling as well as simulation of photonic crystal designs are introduced. The modeling techniques include finite difference time domain (FDTD) method and Plane Wave Expansion (PWE) method. The FDTD method has been represented in context to modal and polarization properties of the photonic design and PWE method has been represented in context to band gap analysis of the designed photonic structure.

Then a short review of Photonic band gap crystals as well as the some essential basics of photonic crystal fibers material modeling and then proceeds to a discussion on the guiding mechanism including modified total internal reflection and photonic band gap guidance are reviewed. The main properties of solid core PCFs that includes dispersion tailoring, ultra high nonlinearities, birefringent features are being studied. A short review of the loss mechanisms is also presented.

The FDTD modeling of photonic crystal waveguide in different materials is done by taking the rectangular lattice waveguide structure and dielectric material of user defined constant refractive index. The default material is taken to be air with unit refractive index. The FDTD simulation and analyses of modeled crystal is done that presents the reflectance and transmittance properties of the photonic band gap crystal-the electric and magnetic field component for transverse electric polarization and the poynting vector also. The band gap analysis for the modeled photonic crystal is done by PWE method by taking a same tolerance factor for all the materials simulations and thus band gaps are located and analyzed.

TABLE OF CONTENTS

LIST OF FIGURES Page No.

LIST OF TABLES PAGE NO.

CHAPTER

1 INTRODUCTION

The last century has been the age of artificial materials. One material that stands out in this regard is the semiconductor. Revolution in the electronics industry in the 20th century was made possible by the ability of semiconductors to microscopically manipulate the flow of electrons. Further advancement in the field prompted scientists to suggest that the new millennium will be the age of photonics in which artificial materials will be synthesized to microscopically manipulate the flow of light. One of these will be photonic band gap (PBG) materials having periodic dielectric structure.

The study of distributed feedback lasers has been reported on the basis of the fact that propagation of electromagnetic waves as well as that of light is forbidden for a small range of wave vectors and the index contrast is typically of the order of $n_a/n_b = 0.01$. However, the contrast is too low for fabrication of photonic crystals, which are new materials where photons are used instead of electrons as the information carrier. Some hybrid optoelectronic circuits have produced significant improvements over the performance of electronic circuits. However, there is a need for multipurpose photonic integrated circuits analogous to electronic integrated circuits to work at micrometre wavelength scale (1– 10 mm), because light has many advantages over electricity; for instance, it can travel in dielectric materials at much greater speeds and carry larger amounts of information per second. The bandwidth of dielectric materials (of the order of one terahertz for fibre optics communication) provides space for larger amount of information as compared to a few hundred kHz for present telephone.

1.1 Introduction

Optical fibers, integrated optical waveguides and a plethora of associated devices and systems are today finding wide use in areas covering telecommunications, sensor technology,

medicine, and spectroscopy. The operation of such devices is usually based on the well-known effect of index guiding which assures controlled transmission of light in dielectric or semiconductor materials. This effect has been exploited for many years and the technology based on it is now approaching its limits of physical performance. Only very recently research on new materials has opened up the possibilities of guiding and controlling light by an entirely new photonic bandgap (PBG) effect. This discovery has created a huge interest in photonic crystals, the novel materials utilizing the PBG effect. It has been predicted that their utilization will soon have a major impact on a wide range of photonic applications [1].

The photonic phenomenon has relied, in general, on the mechanism of total internal reflection. Light propagating in materials of high refractive index is reflected at the interface in materials of low refractive index, and requires an optically smoother interface with respect to wavelength. This requirement limits the degree of miniaturization of optical components, which necessitates a different mechanism from total internal reflection to fabrication of photonic crystals. The underlying concept is based on the existence of the PBG. In a nutshell, the idea is to design materials which can affect the properties of photons similar to the way ordinary semiconductor crystals affect the properties of electrons, and to discuss their physics and novel practical applications ranging from clinical medicine to information technology.

One of the most important applications is Photonic Computing. Currently, computers process information in binary units by identifying an electric charge, or the absence thereof, as being a “one” or a “zero.” This allows the computer to calculate at a rate of 2^x bpt (bits per unit time), with ‘x’ being the current limit across the system bus. However, the use of Photonic computing could easily increase the rate of computing power to 16^x bpt. For example, the current limit for most desktop computers is 32 bpt, so the total output is 2^{32} bpt, or 4,294,967,296 bpt[2]. While that may seems rather fast, the same computer utilizing Photonic Computing Technology would output information at a rate of 16^{32} or 340,282,366,920,938,463,463,374,607,431,770,000,000 bpt. This is 79,228,162,514, 264,337,593,543,950,336 times more powerful than most desktop computers.

To accomplish this, an IO device in a Photonic system must first be given a specific light wave frequency range in order to communicate with the CPU (similar to how the Interrupt

Request settings work in most PCs). This frequency will allow the computer to know which IO device the incoming information is from. This frequency is further divided into 16 subsequent ranges, each representing a different hexadecimal digit. This allows the device to communicate directly in hexadecimal digits, without needing to translate to binary.

The device will then send the information to the CPU in the form of photons. For example, if the device were a keyboard sending the following hexadecimal value "78AE6C," a total of 6 photons would be sent to the CPU, each at a different light frequency, but each one being within the limits of that device. This information will then travel at the speed of light through the connecting medium (typically optic fiber) until it reaches the processing chip.

The processor will then identify the incoming IO source by the photon's frequency range, and will then interpret the value of the photon by the same method. The processor can than carry on processing the information in hexadecimal digits rather than binary. The diagram below summarizes this process.

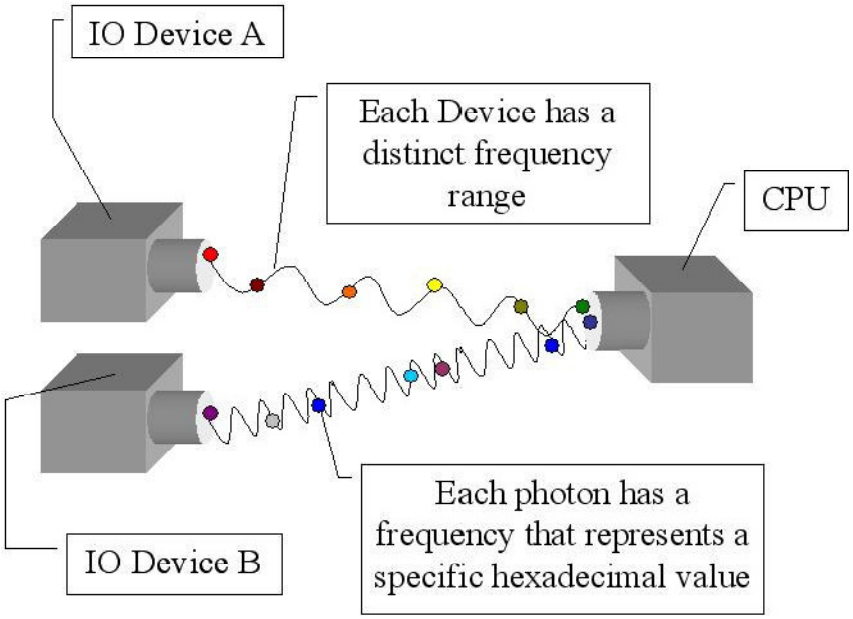

Figure 1(a): Photonic Computing [2]

Photonic Computing not only increases the speed of data transmission, but also dramatically increases the quantity of information being transmitted. The limits of computational power have yet again stretched far beyond anything previously imagined.

1.2 Multi Processor Computing System on Chips

Driven by the advances of semiconductor technology, future System on chips (SoCs) will continue to accelerate in system's complexity and capacity. SoCs in the next decade are expected to integrate hundreds, or even more of, processing elements (PEs) and/or storage elements (SEs) on a single chip. SoC designs at this scale cannot be started from scratch, instead, it is common believe that SoCs will be designed using pre-existing components, such as processors, controllers and memory arrays. Future SoC design methodologies have to support component re-use in a plug-and-play fashion in order to meet time-to-market requirement.

In such a plug-and-play system integration approach, the most critical factor will be related to the communication scheme among components. The design of reliable, low-energy and high-performance on-chip communication architectures for future SoCs will pose unprecedented challenges. Interconnect technology will become the limiting factor for achieving the operational goals. Therefore, we envision a communication-centric view of design methodology in the years to come, as 50-100nm technologies will prevail in the second part of this decade.

Traditional on-chip communication structures have already encountered many limitations in today's VLSI designs. Many of these limitations will become even more problematic as the semiconductor technology advances into newer generations. These limitations are either associated with the scaling-down of the device feature size, or they are inevitable with the scaling-up of design complexity. Particularly, the following issues will become the bottleneck in the future communication-centric SoC design scheme:

- Throughput Limitation– Traditional on-chip communication structures (i.e., the buses) cannot scale up as the number of components increases. When multiple data flows are transmitted concurrently, they will compete for the same communication resources.
- Energy Consumption– as the VLSI device features are continuously shrinking down, interconnect wires have been one of the major contributors of the system energy consumption. The buses used in many of today's SoC designs are notoriously not

energy-efficient, because every bit transmitted is propagated throughout the bus to every terminal.

- Signal Integrity – Energy considerations will impose small logic swings and power supplies, most likely below 1 Volt. Smaller device feature sizes will also produce denser wires (i.e., 7 layers or more of routing wires) connecting highly compacted transistors. Therefore, future VLSI systems will become more vulnerable to various forms of electrical noise, such as cross-talk, electro-magnetic interference (EMI) and radiation-induced charge injection (soft errors). An additional source of errors is contention in shared-medium networks. Contention resolution is fundamentally a non-deterministic process, because it requires synchronization of a distributed system, and for this reason it can be seen as an additional noise source. Because of these effects, the mere transmission of digital values on wires will be inherently unreliable.
- Signal Latency– The propagation delay on wires will gradually dominate the signal latency as the wire feature size shrinks. In fact, wire delay has already become a big challenge in today's VLSI systems, because the delay is determined by the physical distribution of the components, which is hard to predict in the early stages of the design flow. A more predictable communication scheme is of great importance in the future SoC designs.
- Global Synchronization– Propagation delay on global wires - spanning a significant fraction of the chip size - will pose another challenge on future SoCs. As the wire size continues to shrink, the signal propagation delay will eventually exceed the clock period. Thus signals on global wires will be pipelined. Hence the need for latency insensitive design is critical. The most likely synchronization paradigm for future chips is globally-asynchronous locally-synchronous (GALS), with many different clocks.

A multiprocessor system with a large number of nodes can be built at low cost by combining the recent advances in high capacity channels available through optical fiber communication. A highly fault tolerant system is created with good performance characteristics at a reduction in system complexity. The system capitalizes on the optical self-routing characteristic of wavelength division multiple accesses to improve performance and reduce complexity. Thus

the electrical, logic, and functional properties of the interconnection scheme can be abstracted.

On-chip optical interconnects can overcome this bottleneck by replacing electrical wires with optical waveguides. In the year 2008 Sudeep Pasricha, Nikil Dutt proposed an optical ring bus (ORB) [3] based on-chip communication architecture for next generation MPSoCs. ORB uses an optical ring waveguide to replace global pipelined electrical interconnects while preserving the interface with today's bus protocol standards such as AMBA AXI. We present experiments to show how ORB has the potential to provide superior performance (more than 2×) and significantly lower power consumption (a reduction of more than 10×) compared to traditionally used pipelined, all-electrical bus-based communication architectures, for 65-22 nm technology nodes.

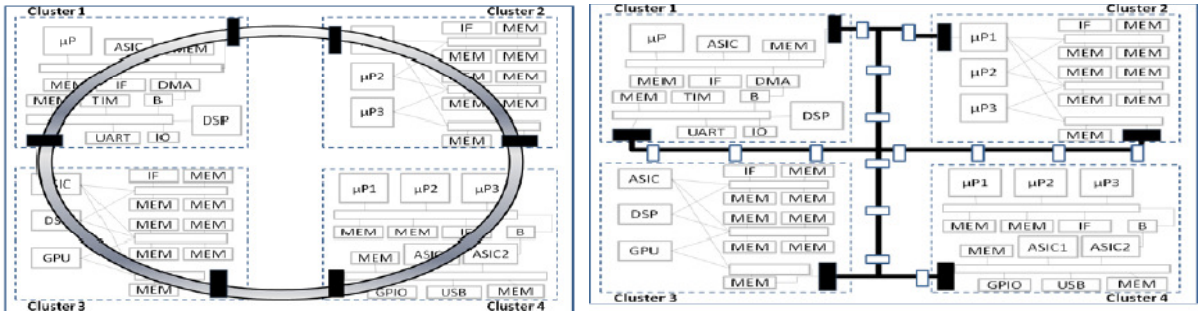

(i) (ii)

Figure 1(b): (i) ORB on-chip communication architecture on MPSOC's (ii) Traditional Multi-cycle pipelined on-chip global communication architecture on MPSOC's [3]

Furthermore, ORB is scalable to accommodate an increasing number of computational clusters and cores on a chip in the future, and provides a clean separation of concerns as the optical waveguide and components are fabricated in a separate, dedicated layer.

1.3 Silicon Photonics

The traditional argument in favor of silicon photonics is based on its compatibility with the mature silicon IC manufacturing. Silicon wafers have the lowest cost (per unit area) and the highest crystal quality of any semiconductor material. The industry is able to produce

microprocessors with hundreds of millions of components, all integrated onto a thumb-size chip, and offer them at such a low price that they appear in consumer electronics. Silicon manufacturing represents the most spectacular convergence of technological sophistication and economics of scale [4].

Creating low-cost photonics for mass-market applications by exploiting the mighty IC industry has been the traditional motivation for silicon photonics researchers. Another motivation is the availability of high-quality silicon-on-insulator (SOI) wafers, an ideal platform for creating planar waveguide circuits. The strong optical confinement offered by the high index contrast between silicon (n = 3.45) and SiO2 (n = 1.45) makes it possible to scale photonic devices to the hundreds of nanometer level. Such lateral and vertical dimensions are required for true compatibility with IC processing. In addition, the high optical intensity arising from the large index contrast (between Si and SiO2) makes it possible to observe nonlinear optical interactions, such as Raman and Kerr effects, in chipscale devices. This fortuitous outcome has enabled optical amplification, lasing, and wavelength conversion, functions that until recently were perceived to be beyond the reach of silicon. The above arguments represent the traditional and still valid motivation in favor of silicon photonics

2010 marks the 50th anniversary of the laser and 51st anniversary of the IC. The best aspects of these revolutionary technologies that shaped the latter half of the 20th century are now being combined to fuel the prospects of innovation for the 21st century. By bringing together the high speed, long distance communication attributes of lasers with the low cost, scalable manufacturing process of silicon, Intel Labs' [5] Silicon Photonics researchers are setting the stage for the performance, communication and design possibilities of tomorrow's technologies.

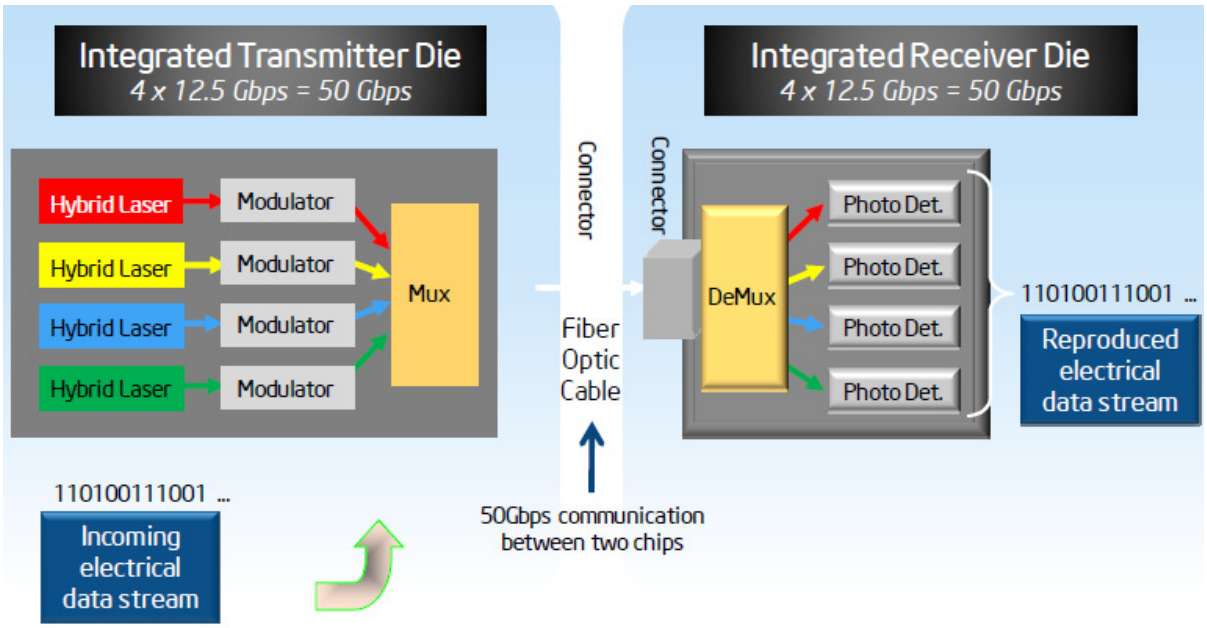

Figure 1(c): Complete silicon photonic trance-receiver system [5]

However, silicon has proved to be the best material for infrared, and near infrared wavelengths. With increase in demand and thus increase in bandwidth time is not far when we have to use the far infrared waves for communication purposes. Thus we look in for FDTD modeling of different materials on photonic band gap scale on 1900 nm wave.

1.4 FDTD Modeling

The photonic devices that include photonic crystal, photonic crystal fibers and PCFs sensors etc, in this context are modeled by several numerical modeling techniques. The modeling includes the device design or layout, the modal properties like the reflectance and transmittance analysis and the band gap analysis in case of photonic band gap devices. All these properties are necessary to analyse a photonic device in order to use it for a specific application e.g. modeling of photonic crystal fiber is necessary to use it in PCFs sensors. So the Accurate modeling of photonic devices is essential for the development of new as well as higher performance optical components and applications.

Computational electrodynamics or electromagnetic modeling is the process of modeling the interaction of electromagnetic fields with physical objects and the environment. It typically

involves using computationally efficient approximations to Maxwell's equations and is used to calculate and analyse the electromagnetic wave propagation when not in free space. Many finite difference based numerical modeling methods have been developed in the past three decades. Typical among them are the finite difference time domain method of Yee's scheme, the transmission line matrix method, the multi resolution time domain method, and the unconditionally stable finite difference time domain methods. All these methods have become powerful tools in solving electromagnetic structure problems, yet their formulations appear to be unrelated. Among these the Finite Difference Time Domain (FDTD) Analysis is a very popular numerical modeling method for solving electromagnetic problems. An increasing number of simulators based on these techniques are being developed commercially, e.g. OptiFDTD by optiwave system that has been used in this research work.

FDTD is a popular computational electromagnetic technique. It is easy to understand and easy to implement in software. Since it is a time-domain method, solutions can cover a wide frequency range with a single simulation run. FDTD belongs in the general class of grid-based differential time-domain numerical modeling methods. Maxwell's equations (in partial differential form) are modified to central-difference equations, discretized, and implemented in software. The equations are solved in a cyclic manner: the electric field is solved at a given instant in time, then the magnetic field is solved at the next instant in time, and the process is repeated over and over again. The FDTD was first introduced as a numerical method in form of space grid and time-stepping algorithm for solving Maxwell's equations by Kane Yee in 1966 [6], and pioneering work on the application of this technique in microwave domain as well as the descriptor "Finite-difference time-domain" and its corresponding "FDTD" acronym were originated by Allen Taflove [7]. Since about 1990, FDTD techniques have emerged as primary means to computationally model many scientific and engineering problems dealing with electromagnetic wave interactions with material structures. Current FDTD modeling applications range from near-DC (ultralow-frequency geophysics involving the entire Earth-ionosphere waveguide) through microwaves (radar signature technology, antennas, wireless communications devices, digital interconnects, biomedical imaging/treatment) to visible light (photonic crystals, nano-plasmonics, solitons, and bio-photonics).

FDTD is in essence an initial-value problem, where an electromagnetic field is allowed to evolve as specified by the sources, in discrete time steps along a lattice including the structure to be analyzed. The evolution of the field is determined by the complex dielectric constants at each cell. At boundaries with differing dielectric constants, reflection, refraction and diffraction can be observed. The time-stepping is usually carried out to several complete cycles of a sinusoidaly varying source, and maximum values of the field component magnitudes during a half-cycle after the last complete cycle are stored. In this way, a steady-state solution [7] is achieved, provided the wave is allowed to propagate through the whole model space.

In the analysis, great care must be taken in choosing the boundary conditions. Since FDTD is an initial value time domain method, the propagating wave will reflect at the lattice boundaries unless special conditions are imposed on the fields at the boundary cells to make them non-reflecting i.e. absorbing. Although the absorbing boundaries [7] extend the limits of the lattice and thus reduce space of the structure to be analyzed, FDTD presents savings in memory and execution time whereas other methods require storage and computation time on the order of $(3N)^2$ and $(3N)^3$ respectively, where N is the number of cells in the model. FDTD requires only N for both. This is a direct consequence of the time domain aspect of the method. The structure analyzed with FDTD can include features down to one cell in size. This is an important advantage in the analysis of near-field effects. Since the lattice is usually made of cells in the order of a tenth of wavelength, features of a few tens of nanometers can be included in models in the optical region. These features can be sources, or absorbers and scatterers.

In order to use FDTD a computational domain must be established. The computational domain is simply the physical region over which the simulation will be performed. The E and H fields are determined at every point in space within that computational domain. The material of each cell within the computational domain must be specified. Typically, the material is either free-space (air), metal or dielectric. Any material can be used as long as the permeability, permittivity, and conductivity are specified. Once the computational domain and the grid materials are established, a source is specified. The source can be an impinging plane wave, a current on a wire, or an applied electric field, depending on the application.

Since the E and H fields are determined directly, the output of the simulation is usually the E or H field at a point or a series of points within the computational domain. The simulation evolves the E and H fields forward in time. Processing may be done on the E and H fields returned by the simulation. Data processing may also occur while the simulation is ongoing. While the FDTD technique computes electromagnetic fields within a compact spatial region, scattered and/or radiated far fields can be obtained via near-to-far-field transformations. FDTD is a versatile modeling technique used to solve Maxwell's equations. It is intuitive, so users can easily understand how to use it and know what to expect from a given model. FDTD is a time-domain technique, and when a broadband pulse is used as the source, then the response of the system over a wide range of frequencies can be obtained with a single simulation. This is useful in applications where resonant frequencies are not exactly known, or anytime that a broadband result is desired. Since FDTD calculates the E and H fields everywhere in the computational domain as they evolve in time, it lends itself to providing animated displays of the electromagnetic field movement through the model. This type of display is useful in understanding what is going on in the model, and to help ensure that the model is working correctly. The FDTD technique allows the user to specify the material at all points within the computational domain. A wide variety of linear and nonlinear dielectric and magnetic materials can be naturally and easily modeled. FDTD allows the effects of apertures to be determined directly. Shielding effects can be found, and the fields both inside and outside a structure can be found directly or indirectly. FDTD uses the E and H fields directly. Since most electromagnetic modeling applications are interested in the E and H fields, it is convenient that no conversions must be made after the simulation has run to get these values.

Since FDTD requires that the entire computational domain be gridded, and the grid spatial discretization must be sufficiently fine to resolve both the smallest electromagnetic wavelength and the smallest geometrical feature in the model, very large computational domains can be developed, which results in very long solution times. Models with long, thin features like wires are difficult to model in FDTD because of the excessively large computational domain required. There is no way to determine unique values for permittivity and permeability at a material interface. FDTD finds the E/H fields directly everywhere in the computational domain. If the field values at some distance are desired, it is likely that this

distance will force the computational domain to be excessively large. Far-field extensions are available for FDTD, but require some amount of post processing. Since FDTD simulations calculate the E and H fields at all points within the computational domain, the computational domain must be finite to permit its residence in the computer memory. In many cases this is achieved by inserting artificial boundaries into the simulation space. Care must be taken to minimize errors introduced by such boundaries. There are a number of available highly effective absorbing boundary conditions (ABCs) to simulate an infinite unbounded computational domain. Most modern FDTD implementations instead use a special absorbing "material", called a perfectly matched layer (PML) to implement absorbing boundaries [7]. Because FDTD is solved by propagating the fields forward in the time domain, the electromagnetic time response of the medium must be modeled explicitly. For an arbitrary response, this involves a computationally expensive time convolution, although in most cases the time response of the medium can be adequately and simply modeled using the recursive convolution (RC) technique, the auxiliary differential equation (ADE) technique or the Z-transform technique. An alternative way of solving Maxwell's equations that can treat arbitrary dispersion easily is the Pseudo spectral Spatial-Domain method (PSSD), which instead propagates the fields forward in space.

Interest in FDTD Maxwell's equations solvers has increased nearly exponentially over the past 20 years. Increasingly, engineers and scientists in nontraditional electromagnetics related areas such as photonics and nanotechnology have become aware of the power of FDTD techniques. Notwithstanding the overall expansion of interest in all Computational electromagnetic techniques, there are some primary reasons for the tremendous expansion of interest in FDTD computational solution approaches for Maxwell's equations. Some of these are as follows:

- FDTD uses no linear algebra. Being a fully explicit computation, FDTD avoids the difficulties with linear algebra that limit the size of frequency-domain integral-equation and finite-element electromagnetics models.
- FDTD is accurate and robust. The sources of error in FDTD calculations are well understood, and can be bounded to permit accurate models for a very large variety of electromagnetic wave interaction problems.

- FDTD treats impulsive behavior naturally. Being a time-domain technique, FDTD directly calculates the impulse response of an electromagnetic system.
- FDTD is a systematic approach. With FDTD, specifying a new structure to be modeled is reduced to a problem of mesh generation rather than the potentially complex reformulation of an integral equation.
- Parallel-processing computer architectures have come to dominate supercomputing. FDTD scales with high efficiency on parallel-processing CPU-based computers, and extremely well on recently developed GPU-based accelerator technology.

These factors combine to indicate that FDTD will likely remain one of the dominant computational electrodynamics techniques for numerical modeling of photonic and related devices.

FDTD method has been used extensively in the analysis of electrically large structures in the microwave domain, but has only recently been applied to optical problems. Because of memory limitations of computers used, the method is generally restricted to configurations which extend to the order of tens of wavelengths in three dimensions, or hundreds of wavelengths in two dimensions. Optical sensor structures however are of suitable size to be modeled with FDTD and the advantages of the technique become pronounced especially in the design of photonic sensors which employ evanescence or near-field effects. Among these is the possibility to incorporate the distribution of the analyte on the sensing surface as well as the optical characteristics of the sensor in the optical model. Although the computer resources required for arbitrary structures in three dimensions can limit the scope of analyses, it is relatively simple to use symmetry properties of the structures to relax these requirements. In addition, for planar structures, two-dimensional models are adequate for studying many aspects of sensor design. Recently, FDTD has been applied in the optical range of frequencies, as suitable problems to be analyzed with the method have emerged. Planar optical sensors are particularly good candidates for modeling with FDTD. Their structure is simple enough for the model to be used effectively, and due to the planarity only a two-dimensional analysis is required for many cases. With a modern day supercomputer, structures of hundreds of wavelengths long can be analyzed in two dimensions.

1.5 Motivation

The use of silicon has long been established for infrared optics, such as simple lenses and windows and long-wave detection. Today (in 2011) silicon is the material of choice for visible detection, particularly as the imaging element in digital cameras. In some commercial cameras, the wavelength response of silicon has even been extended to the near infrared (to 1,100nm). In addition, the vast expert base in silicon materials, device physics, and processing equipment that has been developed for electronic microcircuits, lay in waiting to address the rapid growth of the fiber optic infrastructure for the transport of information, video, and voice. There is no doubt about the economic and technical advantages of silicon and it was inevitable that silicon would be employed wherever optic fiber is deployed. Predictably, with the rise in Internet and data transmission, the need for higher speed, broader bands, and lower cost matches all four of the material benefits provided by silicon.

Silicon material and processing methods, thanks to the huge microelectronics' industry, has a level of purity and maturity far exceeding any other. Extending this materials capability to photonics and also merging the two primary device types, photonics and electronics, into one integrated dual functional device brings the benefits of a large economy of scale and wide application far beyond the simple combination of separate devices.

With research growing in numerous industrial laboratories, one expects to son to be commercially available, 100Gbps devices for optical communication and novel devices for sensors and transduction.

The device physics of semiconductor photonics and electronics and the interaction between the two is an open field for discovery and invention. Bring new challenges to the device engineer in design, processing, and packaging.

1.6 Thesis Organization

Chapter 2 is mainly concerned with the numerical modeling techniques of photonic crystal designs. The chapter starts with the basics of FDTD method and then the FDTD equations are described for two and three dimensional space. Various absorbing boundary conditions are also described following the FDTD equations. After that FDTD algorithm has been

explained for the Telegrapher's partial difference equations. Chapter also includes the plane wave expansion method for the band gap analysis of photonic crystal structures. The PWE equations are solved to describe the dispersion relationship between the frequencies of the modes and wave vector k that usually plotted in form of band diagram.

Chapter 3 starts with a literature review of photonic band gap crystals, starting from basics to the advancement towards the photonic crystal fibers. After that major guiding mechanisms of the photonic crystal fiber are described. The unique properties of the PBG crystals that make it prime choice for the photonic applications are also included in the chapter. At last various loss mechanisms are also described in this chapter.

Chapter 4 concentrates on the modeling and simulation of the photonic crystal as well as the photonic crystal fiber. After simulating the designs FDTD analysis is done firstly to describe the transmittance and reflectance properties of the photonic band gap crystal using different materials. The band diagrams of the designs are plotted and band gaps are located and analyzed by PWE band solver and in the end the band gaps of designs are summarized that gives the frequency range of the input for which wave get strongly reflected in the designed photonic structure.

Finally, a conclusion of the thesis is given in **chapter 5.**

CHAPTER 2

FINITE DIFFERENCE TIME DOMAIN TECHNIQUE

Numerical simulations play an important role for the design and modeling of photonic crystal structures. So far, various modeling methods [8] in which not only a full-vector model but also an approximate scalar model is used have been developed such as effective index approach , plane-wave expansion (PWE) method , localized-function method, multipole method (MM), beam propagation method (BPM), finite-difference method (FDM), finite difference time-domain method (FDTD), boundary element method (BEM), and finite-element method (FEM). An approximate-scalar model is a valuable tool for aiding fabrication efforts because it is easy to use and provides good qualitative information. However, in order to model photonic crystal structures especially PCFs accurately, it is crucial to use a full-vector model [8].

In particular, a complete vector model is necessary for predicting sensitive quantities such as dispersion and birefringence. The choice of modeling method can impact the computational time, required computational resources, and limitations of the methods, so it is important to explore the usefulness and limitations of each method.

2.1 Introduction

The FDTD method [9] belongs in the general class of grid based differential time domain numerical modeling methods. The time-dependent Maxwell's equations in partial differential form are discretized using central-difference approximations to the space and time partial derivatives. The resulting finite-difference equations are solved in either software or hardware in a leapfrog manner: the electric field vector components in a volume of space are solved at a given instant in time; then the magnetic field vector components in the same spatial volume are solved at the next instant in time; and the process is repeated over and

over again until the desired transient or steady-state electromagnetic field behavior is fully evolved. Virtually any physical system that is governed by a time-dependent partial differential equation (PDE) can be readily simulated through the use of FDTD.

The FDTD method has been established as a powerful engineering tool for integrated and diffractive optics device simulations. This is due to its unique combination of features, such as the ability to model light propagation, scattering and diffraction, and reflection and polarization effects. It can also model material anisotropy and dispersion without any pre-assumption of field behavior such as the slowly varying amplitude approximation. The method allows for the effective and powerful simulation and analysis of sub-micron devices with very fine structural details. A sub-micron scale implies a high degree of light confinement and correspondingly, the large refractive index difference of the materials, mostly semiconductors to be used in a typical device design.

2.1.1 Basics

The basic of FDTD method starts with solving Maxwell equations in heterogeneous materials [10]. The procedure begins with two basic equations as described below.

$$\nabla \times E = -\mu \frac{\partial \vec{H}}{\partial t} \qquad (1)$$

$$\nabla \times H = \sigma \vec{E} + \varepsilon \frac{\partial \vec{E}}{\partial t} \qquad (2)$$

Where $\varepsilon = \varepsilon_0 \varepsilon_r$, is the dielectric permittivity and μ is the magnetic permeability of the vacuum. The refractive index is, $n = \sqrt{\varepsilon_r}$. Equation (1) represents the Ampere's law [10] and equation (2) represents the Faraday's law [10]. The first step is to convert the vector differential equations represented by (1) and (2) to the scalar differential equations. As we know

$$\nabla = \frac{\partial}{\partial x}\hat{x} + \frac{\partial}{\partial x}\hat{y} + \frac{\partial}{\partial x}\hat{z} \qquad (3)$$

Putting the value in (1), it becomes

$$\begin{bmatrix} \hat{x} & \hat{y} & \hat{z} \\ \partial/\partial x & \partial/\partial y & \partial/\partial z \\ E_x & E_y & E_z \end{bmatrix} = -\mu\left(\frac{\partial H_x}{\partial t}\hat{x} + \frac{\partial H_y}{\partial t}\hat{y} + \frac{\partial H_z}{\partial t}\hat{z}\right) \qquad (4)$$

Solving right hand side of above equation we get

$$\hat{x}\left(\frac{\partial E_z}{\partial y} - \frac{\partial E_y}{\partial z}\right) - \hat{y}\left(\frac{\partial E_z}{\partial x} - \frac{\partial E_x}{\partial z}\right) + \hat{z}\left(\frac{\partial E_y}{\partial x} - \frac{\partial E_x}{\partial y}\right) = -\mu\left(\frac{\partial H_x}{\partial t}\hat{x} + \frac{\partial H_y}{\partial t}\hat{y} + \frac{\partial H_z}{\partial t}\hat{z}\right) \qquad (5)$$

Now we will be able to express equation (5) in form of three scalar differential equations by equating the coefficients of $\hat{x}, \hat{y}, \hat{z}$ as

$$\frac{\partial E_z}{\partial y} - \frac{\partial E_y}{\partial z} = -\mu\frac{\partial H_x}{\partial t} \qquad (6)$$

$$\frac{\partial E_z}{\partial x} - \frac{\partial E_x}{\partial z} = \mu\frac{\partial H_y}{\partial t} \qquad (7)$$

$$\frac{\partial E_y}{\partial x} - \frac{\partial E_x}{\partial y} = -\mu\frac{\partial H_z}{\partial t} \qquad (8)$$

These equations had derivatives in both space and time. Similarly the faraday's law represented by equation (2) can be represented in form of scalar differential equations as

$$\frac{\partial H_z}{\partial y} - \frac{\partial H_y}{\partial z} = \sigma E_x + \varepsilon\,\frac{\partial E_x}{\partial t} \qquad (9)$$

$$-\left(\frac{\partial H_z}{\partial x} - \frac{\partial H_x}{\partial z}\right) = \sigma E_y + \varepsilon\,\frac{\partial E_y}{\partial t} \qquad (10)$$

$$\frac{\partial H_y}{\partial x} - \frac{\partial H_x}{\partial y} = \sigma E_z + \varepsilon\,\frac{\partial E_z}{\partial t} \qquad (11)$$

Discretizing the FDTD grid

The next step is to convert the scalar differential equations to the difference equations and this is done by discretizing the 3-D FDTD grid. The FDTD grid is shown in the figure below

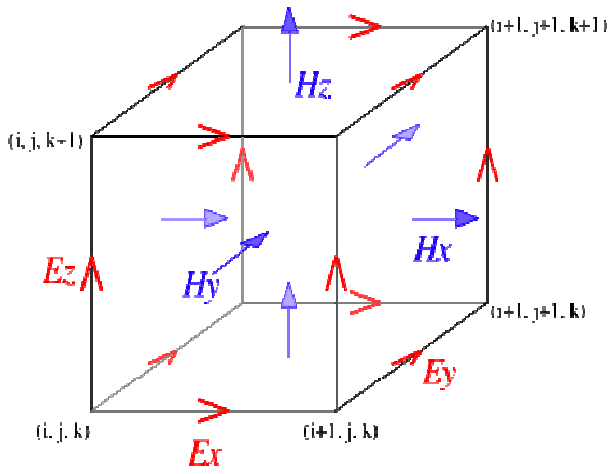

Figure 2(a): FDTD grid showing E and H components [10].

The electric field and magnetic field components are shown in the grid. We can convert each scalar differential equation into the difference equation in terms the field components as well as space and time steps. Taking equation (8) the left hand side of the equation becomes

$$\left(\frac{E_y(i+1j,k)-E_y(i,j,k)}{\Delta x}\right)-\left(\frac{E_x(i,j+1,k)-E_x(i,j,k)}{\Delta y}\right)$$

Now from this difference term representing RHS of equation (8).the location of H_z is (i, j, k). To represent LHS of same equation let us consider the time derivative. For this the division of electric field and magnetic field in time is presented as

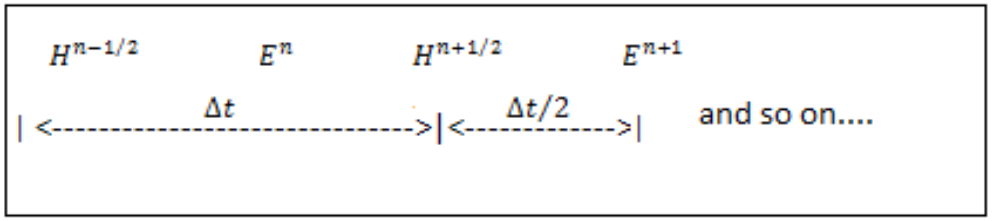

Figure 2(b): Time division of electric and magnetic field components [10]

So it is shown that magnetic field components are at ½ time steps and electric field components are at full time steps. Now if we consider electric field of above equation at nth time step then the complete difference equation becomes

$$\left(\frac{E_y^n(i+1,j,k)-E_y^n(i,j,k)}{\Delta x}\right)-\left(\frac{E_x^n(i,j+1,k)-E_x^n(i,j,k)}{\Delta y}\right) = \mu(i.j,k)\left(\frac{H_z^{n+1/2}(i,j,k)-H_z^{n-1/2}(i,j,k)}{\Delta t}\right) \quad (12)$$

Similarly the other two electric field scalar differential equations can be represented in terms of difference equation discretized in space and time.

Next task is to convert magnetic field scalar differential equations to the same form as the electric field equations are represented. Considering the same time division the LHS of equation (10) becomes

$$-\left[\left(\frac{H_z(i,j,k)-H_z(i-1,j,k)}{\Delta x}\right)-\left(\frac{H_x(i,j,k)-H_x(i,j,k-1)}{\Delta z}\right)\right]$$

The position of E_y will now be (i, j, k) and to find the RHS of the equation, considering the magnetic field at $H^{n+1/2}$ the complete equation becomes

$$-\left[\left(\frac{H_z^{n+1/2}(i,j,k)-H_z^{n+1/2}(i-1,j,k)}{\Delta x}\right)-\left(\frac{H_x^{n+1/2}(i,j,k)-H_x^{n+1/2}(i,j,k-1)}{\Delta z}\right)\right] = \sigma(i,j,k)\left(\frac{E_n+E_{n+1}}{2}\right)+\left(\frac{E_y^{n+1}(i,j,k)-E_y^n(i,j,k)}{\Delta t}\right) \quad (13)$$

So the values of electric and magnetic fields are updated from their previous values to define a crystal lattice that contains a defined number of FDTD grids. The magnetic field and electric field difference equations are also known as FDTD equations in context to the FDTD method. Since these equations are defined for a single grid, we can use them to define 1D, 2D, 3D crystal consisting of the same grids.

2.1.2 Two Dimensional FDTD Equations

The FDTD approach is based on a direct numerical solution of the time-dependent Maxwell's curl equations [11].The photonic device is laid out in the X-Z plane. The propagation is along

Z. The Y-direction is assumed to be infinite. This assumption removes all the $\partial/\partial y$derivatives from Maxwell's equations and splits them into two (TE and TM) independent sets of equations. The 2D computational domain is shown in Figure 2(c). The space steps in the X and Z directions are Δx and Δz, respectively. Each mesh point is associated with a specific type of material and contains information about its properties such as refractive index, and dispersion parameters [12].

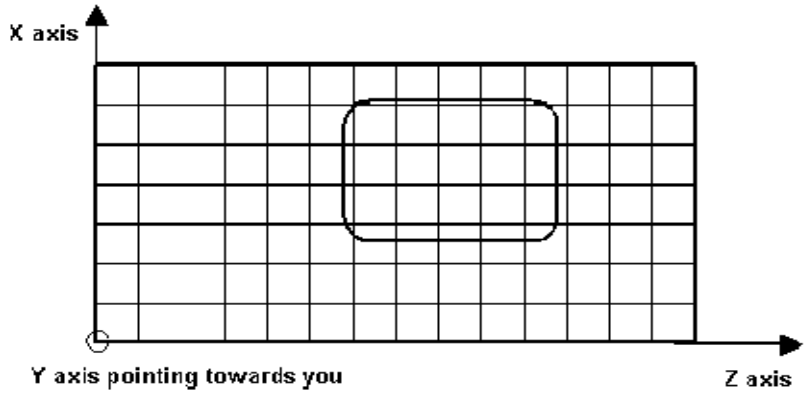

Figure 2(c): The 2-D computational domain [12].

TE waves

In the 2D TE case where H_x, E_y, H_z are nonzero components, propagation is along Z and transverse field variations along X, in lossless media, Maxwell's equations take the following form

$$\mu \frac{\partial H_x}{\partial t} = \frac{\partial E_y}{\partial z} \qquad (a)$$

$$\mu \frac{\partial H_z}{\partial t} = -\frac{\partial E_y}{\partial x} \qquad (b) \qquad (14)$$

$$\varepsilon \frac{\partial E_y}{\partial t} + \sigma E_y = \frac{\partial H_x}{\partial z} - \frac{\partial H_z}{\partial x} \qquad (c)$$

where $\varepsilon = \varepsilon_0 \varepsilon_r$is the dielectric permittivity and μ is the magnetic permeability of the vacuum. The refractive index is $n = \sqrt{\varepsilon_r}$.

Each field is represented by a 2D array as E_y (i, k), H_x (i, k) and H_z (i, k) corresponding to the 2D mesh grid given in Figure 2(c). The indices i and k account for the number of space steps in the X and Z direction, respectively. In the case of TE, the location of the fields in the mesh is shown in Figure 2(d) below.

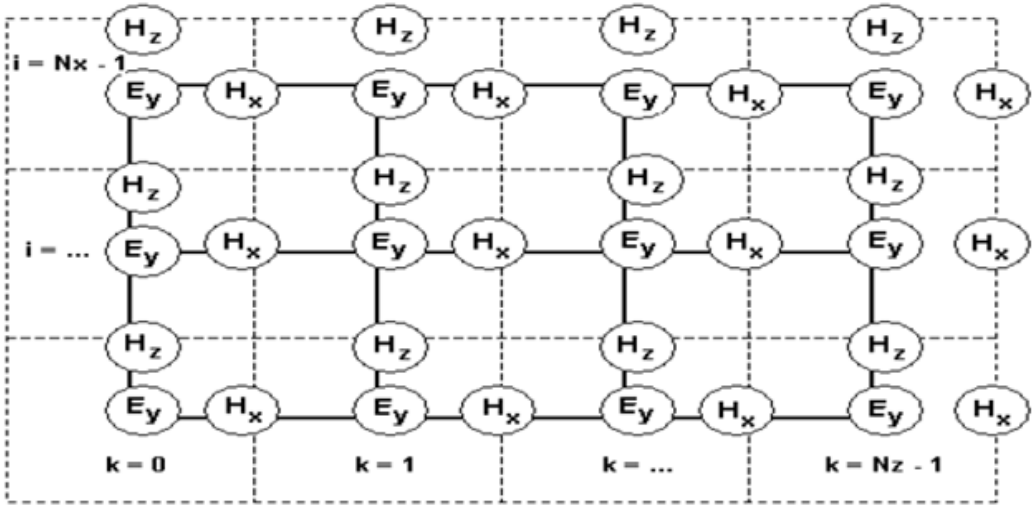

Figure 2(d): Location of the TE fields in the computational domain [12].

The TE fields stencil can be explained as follows. The E_y field locations coincide with the mesh nodes given in Figure 2(c). In Figure 2(d), the solid lines represent the mesh given in Figure 2(c). The E_y field is considered to be the center of the FDTD space cell. The dashed lines form the FDTD cells. The magnetic fields H_x and H_z are associated with cell edges. The locations of the electric fields are associated with integer values of the indices i and k. The H_x field is associated with integer i and (k + 0.5) indices. The H_z field is associated with (i + 0.5) and integer k indices.

The indices i and k label the space steps and along the x and z directions, respectively. This is the so-called Yee's numerical scheme [12] applied to the 2D TE case. It uses central difference approximations for the numerical derivatives in space and time, both having second order accuracy. The sampling in space is on a sub-wavelength scale [13]. Typically, 10 to 20 steps per wavelength are needed. The sampling in time is selected to ensure numerical stability of the algorithm. The time step is determined by the Courant limit:

$$\Delta t \leq 1/\left(c\sqrt{1/(\Delta x)^2 + 1/(\Delta z)^2}\right) \qquad (14\{i\})$$

TM waves

In the 2D TM case where E_x, H_y and E_z are nonzero components, propagation along Z and transverse field variations along X, in lossless media, Maxwell's equations take the following form:

$$\mu\frac{\partial H_y}{\partial t} = \frac{\partial E_z}{\partial x} - \frac{\partial E_x}{\partial z} \qquad (a)$$

$$\varepsilon\frac{\partial E_x}{\partial t} + \sigma E_x = -\frac{\partial H_y}{\partial z} \qquad (b) \qquad (15)$$

$$\mu\frac{\partial E_z}{\partial t} + \sigma E_z = \frac{\partial H_y}{\partial x} \qquad (c)$$

The location of the TM fields in the computational domain follows the same philosophy and is shown in Figure 2(e) below.

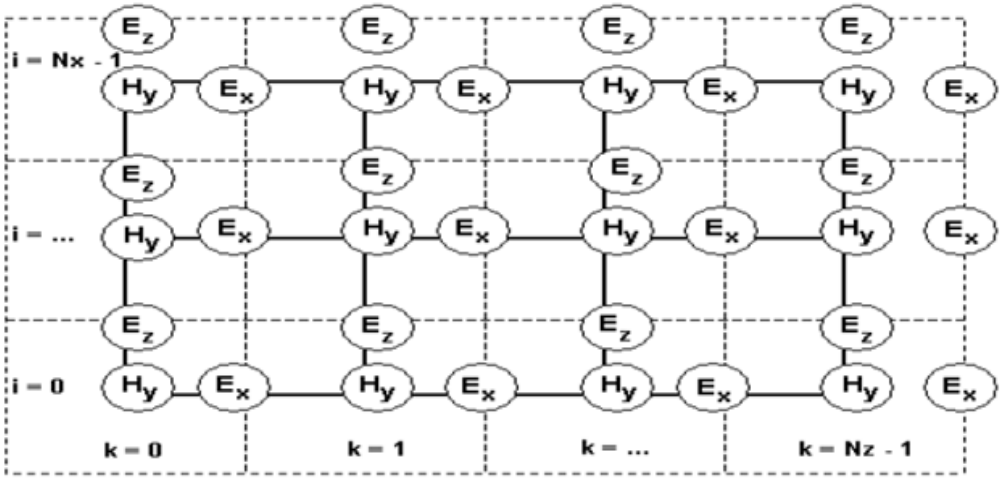

Figure 2(e): Location of the TM fields in the computational domain [12].

Now, the electric field components E_x and E_z are associated with the cell edges, while the magnetic field H_y is located at the cell center. The TM algorithm can be presented in a way

similar to Equation (14). In this way the magnetic field and electric field components are updated accordingly and the grid is continued up to the defined time steps.

2.1.3 Three Dimensional FDTD Equations

In 3D crystal, the lattice structure is a cubic box, the space steps are D_x, D_y and D_z in x, y and z directions respectively.

Each field components is presented by a 3D array $E_x(i, j, k)$, $E_y(i, j, k)$, $E_z(i, j, k)$, $H_x(i, j, k)$, $H_y(i, j, k)$, $H_z(i, j, k)$. The field components position in Yee's Cell are shown in Figure 2(f). These placements and the notation show that the E and H components are interleaved at intervals of 1/2Dh and 1 /2Dt in space and for the purpose of implementing a leapfrog algorithm.

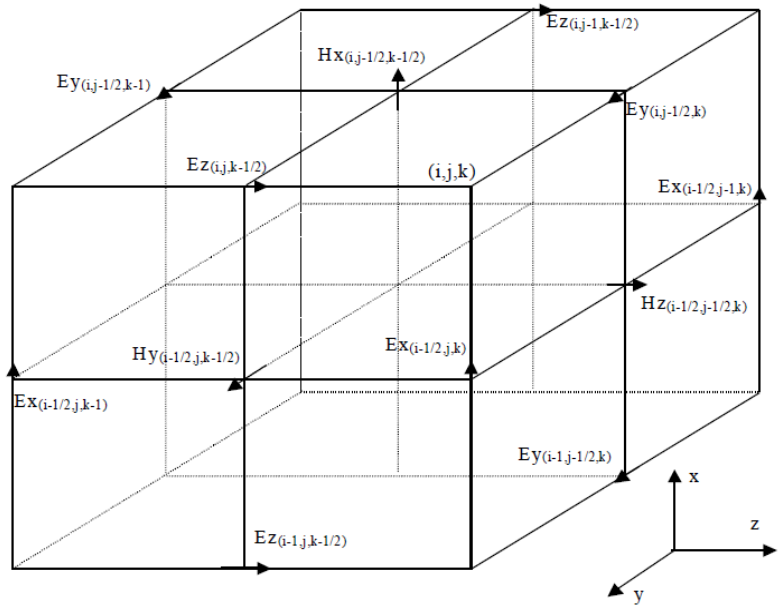

Figure 2(f): Displacement of the electric and magnetic field vector components about a cubic unit cell of the Yee space lattice [12].

Now we can apply the above finite-difference ideas, notations, and field displacements to achieve a numerical approximation of Maxwell's equation. The FDTD equations for electric and magnetic field components can be written as

Equation (16)

$$\mathrm{H_x^{n+1/2}(i,j-1/2,k-1/2)} = \mathrm{H_x^{n-1/2}(i,j-1/2,k-1/2)} + \frac{\Delta t}{\mu \Delta z}\left(\mathrm{E_y^n(i,j-1/2,k)} - \mathrm{E_y^n(i,j-1/2,k-1)}\right) - \frac{\Delta t}{\mu \Delta y}\left(\mathrm{E_z^n(i,j,k-1/2)} - \mathrm{E_z^n(i,j-1,k-1/2)}\right)$$

Equation (17)

$$\mathrm{H_y^{n+1/2}(i-1/2\,,j,k-1/2)} = \mathrm{H_y^{n-1/2}(i-1/2\,,j,k-1/2)} + \frac{\Delta t}{\mu \Delta x}\left(\mathrm{E_z^n(i,j,k-1/2)} - \mathrm{E_z^n(i,j-1,k-1/2)}\right) - \frac{\Delta t}{\mu \Delta z}\left(\mathrm{E_x^n\ (i-1/2\,,j,k)} - \mathrm{E_x^n\ (i-1/2\,,j,k-1)}\right)$$

Equation (18)

$$\mathrm{H_z^{n+1/2}(i-1/2\,,j-1/2\,,k)} = \mathrm{H_z^{n-1/2}(i-1/2\,,j-1/2\,,k)} + \frac{\Delta t}{\mu \Delta y}\left(\mathrm{E_x^n(i-1/2\,,j,k)} - \mathrm{E_x^n(i-1/2\,,j-1,k)}\right) - \frac{\Delta t}{\mu \Delta x}\left(\mathrm{E_y^n\ (i,j-1/2\,,k)} - \mathrm{E_y^n\ (i-1,j-1/2\,,k)}\right)$$

Equation (19)

$$E_x^{n+1}(i-1/2,j,k) = \frac{2\varepsilon - \sigma\Delta t}{2\varepsilon + \sigma\Delta t} E_x^n(i-1/2,j,k) + \frac{2\Delta t}{(2\varepsilon + \sigma\Delta t)\Delta y}\left(H_z^{n+1/2}(i-1/2,j+1/2,k) - H_z^{n+1/2}(i-1/2,j-1/2,k)\right) - \frac{2\Delta t}{(2\varepsilon + \sigma\Delta t)\Delta z}\left(H_y^{n+1/2}(i-1/2,j,k+1/2) - H_y^{n+1/2}(i-1/2,j,k-1/2)\right)$$

Equation (20)

$$E_y^{n+1}(i, j-1/2\,, k) = \frac{2\varepsilon - \sigma\Delta t}{2\varepsilon + \sigma\Delta t} E_y^n(i, j-1/2\,, k) + \frac{2\Delta t}{(2\varepsilon + \sigma\Delta t)\Delta z}\Big(H_x^{n+1/2}(i, j-1/2, k+1/2) - H_x^{n+1/2}(i, j-1/2, k-1/2)\Big) - \frac{2\Delta t}{(2\varepsilon + \sigma\Delta t)\Delta x}\Big(H_z^{n+1/2}(i+1/2, j-1/2\,, k) - H_z^{n+1/2}(i-1/2, j-1/2\,, k)\Big)$$

Equation (21)

$$E_z^{n+1}(i, j, k-1/2) = \frac{2\varepsilon - \sigma\Delta t}{2\varepsilon + \sigma\Delta t} E_z^n(i, j, k-1/2) + \frac{2\Delta t}{(2\varepsilon + \sigma\Delta t)\Delta x}\Big(H_y^{n+1/2}(i+1/2\,, j, k-1/2) - H_y^{n+1/2}(i-1/2\,, j, k-1/2)\Big) - \frac{2\Delta t}{(2\varepsilon + \sigma\Delta t)\Delta y}\Big(H_x^{n+1/2}(i, j+1/2\,, k-1/2) - H_x^{n+1/2}(i, j-1/2\,, k-1/2)\Big)$$

Equation (16) to (21) represented the electric field and magnetic field components in all three directions for the 3D structure that uses these equations to update itself in time as well as space when it is modeled by FDTD method. Hence these equations are the base to model a three dimensional structure in FDTD.

Space Step and Time Step

The fundamental constraint of FDTD method is the step size both for the time and space. Space and time steps relate to the accuracy, numerical dispersion, and the stability of the FDTD method. In general, to keep the results as accurate as possible, with a low numerical

dispersive, the mesh size often quoted is "10 cells per wavelength", meaning that the side of each cell should be 1/10 or less at the highest frequency (shortest wavelength).

The FDTD is a volumetric computational method, so that if some portion of the computational space is filled with penetrable material, the wavelength in the material must be used to determine the maximum cell size.

The following equation is for the suggested mesh size:

$$minimun(\Delta x, \Delta y, \Delta z) = \frac{\lambda_{min}}{10 n_{max}} \qquad (22)$$

Where n_{max} is the maximum refractive index value in the computational domain. Once the cell size is determined, the maximum size for the time step Δt immediately follows the Courant-Friedrichs-Levy (CFL) condition [14].

For 3D FDTD simulation, the CFL condition is:

$$\Delta t \leq \frac{1}{v\sqrt{\frac{1}{(\Delta x)^2} + \frac{1}{(\Delta y)^2} + \frac{1}{(\Delta z)^2}}} \qquad (23)$$

Where *v* is the speed of the light in medium.

For 2D simulations, the above CFL condition can be simplified as:

$$\Delta t \leq \frac{1}{v\sqrt{\frac{1}{(\Delta x)^2} + \frac{1}{(\Delta z)^2}}} \qquad (24)$$

Thus the defined assumptions for space step size and time step size must be considered while defining a two or three dimensional crystal that is to be modeled using FDTD method.

2.2 FDTD Boundary Conditions

The basic FDTD algorithm must be modified at the boundaries of the computational window where suitable numerical absorbing boundary conditions (ABC) are applied. This is one of

the most challenging parts of FDTD simulations. There are several choices for the type of boundary conditions [15]. The Perfectly Matched Layer (PML) boundary conditions have the best performance. Most FDTD simulator uses the Anisotropic PML, or so-called Un-split PML (UPML) version. The UPML boundary conditions are physical rather than numerical because their implementation is based on a Maxwellian formulation rather than on a mathematical model. Their absorbing properties are physically equivalent to the properties of an absorbing uni-axial anisotropic medium with the following permittivity and permeability tensors:

$$\hat{\varepsilon} = \varepsilon \hat{S}, \hat{\mu} = \mu_0 \hat{S}, \hat{S} = \begin{pmatrix} s^{-1} & 0 & 0 \\ 0 & s & 0 \\ 0 & 0 & s \end{pmatrix}, s = \kappa - i \frac{\sigma}{\varepsilon_0 \omega} \qquad (25)$$

A plane wave incident on a half space composed of the above uni-axial medium with an interface in the x that equals constant plane is purely transmitted into it. The reflectionless property is completely independent of the angle of incidence, polarization and frequency of the incident wave. The numerical implementation of the UPML in a 2D (X-Z) computational window requires the introduction of such perfectly matched absorbing layers on all the sides. The corner regions need special attention. In these regions the tensor from Equation (2y) must be modified to:

$$\hat{S} = \begin{pmatrix} s_x^{-1} & 0 & 0 \\ 0 & s_x & 0 \\ 0 & 0 & s_x \end{pmatrix} \begin{pmatrix} s_z & 0 & 0 \\ 0 & s_z & 0 \\ 0 & 0 & s_z^{-1} \end{pmatrix}, s_x = \kappa_x - i \frac{\sigma_x}{\varepsilon_0 \omega}, s_z = \kappa_z - i \frac{\sigma_z}{\varepsilon_0 \omega} \qquad (26)$$

The minimization of the numerical reflectance of the Anisotropic PML layers requires spatial scaling of the conductivity profile from zero (at the interface of the PML) to a maximum value at the end of the computational window:

$$\sigma(x) = \sigma_{max} \left(\frac{x}{L}\right)^m, \quad \kappa(x) = 1 + (\kappa_{max} - 1)\left(\frac{x}{L}\right)^m \qquad (27)$$

Where L is the thickness of Anisotropic PML [30]. Typical values for the parameter *m* are between 2 and 4.

PMC/PEC Boundary Conditions and Plane Wave Simulation

The FDTD simulators have options to use Perfect Electrical Conductor (PEC) and Perfect Magnetic Conductor (PMC) boundary conditions. The boundaries that use the new conditions can be chosen, and Anisotropic PML can be used for the remaining boundaries.

With this PEC/PMC/Anisotropic PML combination, the following simulations may be obtained:

• Plane wave simulation

• Domain reduced simulation for symmetric, periodic, or photonic band gap structures

Image Value of PEC/ PMC

The following graphs show the field set up in the PEC/PMC wall (zero thickness) and its image value

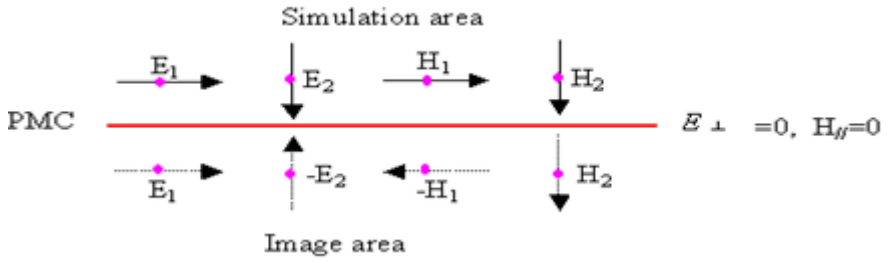

Figure 2(g): Field in PMC and image area [16].

Here $E_{\perp}$ is the vertical electric component in the PMC wall, and is the parallel magnetic component $H_{\parallel}$ in the PMC wall.

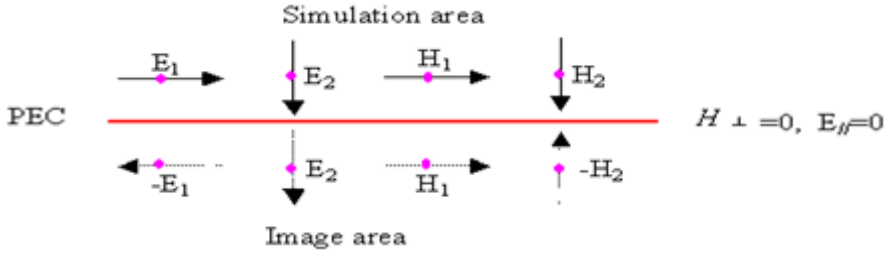

Figure 2(h): Field in PEC and image area [16].

As we can see from Figure 2(g), PMC is a symmetric wall for the symmetric structure with symmetric wave propagation. The following two cases detail the results when PMC occurs.

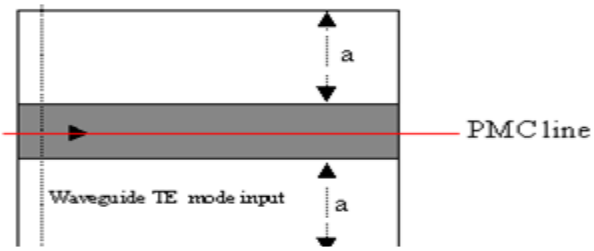

Figure 2(i): PMC wall in a symmetric waveguide excited by symmetric TE waveguide mode

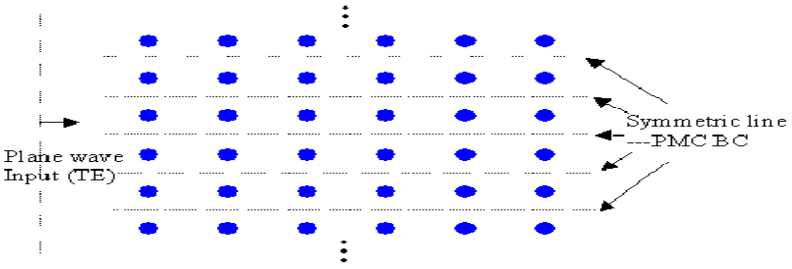

Figure 2(j): PMC wall in a periodic structure for TE plane wave propagation [16].

PMC can be seen as the special case for Bloch's boundary condition [31] (periodic boundary condition) where the k-vector is set to zero in the corresponding direction. PEC line is the complement of PMC, so in Figure 2(i) and Figure 2(j), the PMC line will become the PEC line if the wave polarization is changed to TM.

Plane Wave Realized in Symmetric/Periodic Structure

Figure 2(k) shows how the plane wave simulation can be realized for a symmetric structure. For a 2D TE simulation, the edge of transverse plane should be set to the PMC boundary condition to realize the plane wave.

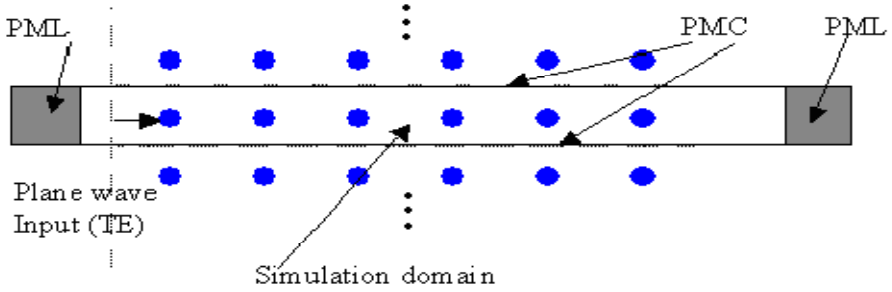

Figure 2(k): Plane wave in TE simulation [16].

For a 2D TM simulation, the edge of transverse plane should set to the PEC boundary condition to realize the plane wave as shown in figure 2(l).

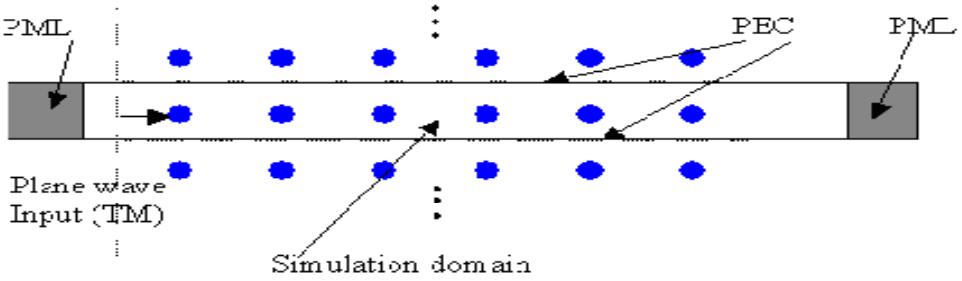

Figure 2(l): Plane wave in TM simulation [16].

For a 3D simulation, the plane wave realization depends on the wave polarization and the boundary condition setup at different edges of the transverse plane. If the wave goes in z-direction, and the input wave is in y-direction polarization, then the y plane (x-z) edge should be set to the PEC and x-plane (y-z plane) edge set to the PMC boundary as shown in figure 2(m).

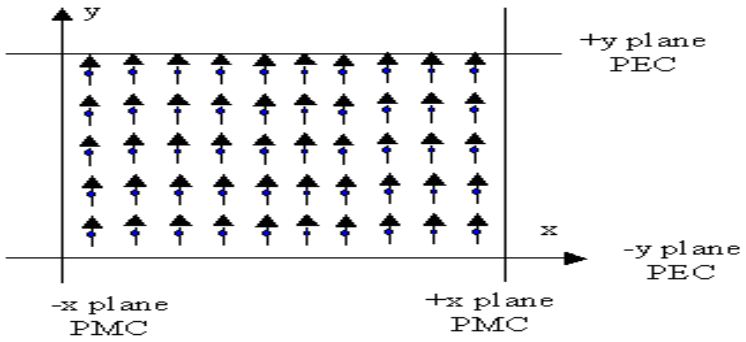

Figure 2(m): Y-polarization plane wave in z-direction of propagation with boundary conditions [16].

For 3D simulation, if the wave goes in z-direction, and the input wave is in x-direction polarization, then the y plane (x-z) edge should be set to the PMC and x-plane (y-z plane) edge set to the PEC boundary as shown in figure 2(n)

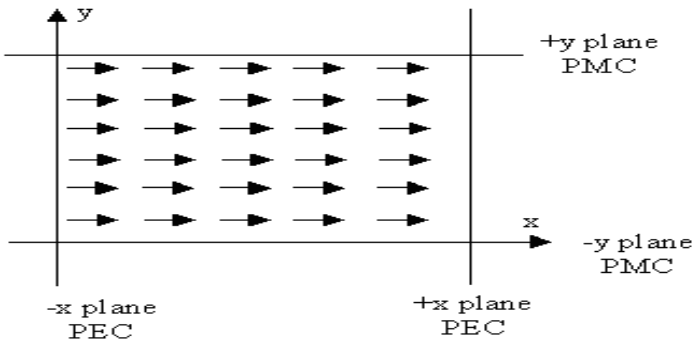

Figure 2(n): X-polarization plane wave in z-direction of propagation with boundary conditions [16].

The plane wave shape can be set by setting the rectangular wave parameters in the Input Wave Properties. Currently, plane wave does not support the tilting angle. Currently, the plane wave simulation is only effective for symmetrical structures [17].

Periodic Boundary Conditions

Some of the FDTD simulators provide the option to use simplified Periodic Boundary Condition (PBC). PBC can work with other boundary conditions such as Anisotropic PML, PMC, and PEC. With PBC, you can generate a simple plane wave simulation or periodic layout simulations.

The simplified PBC [18] is based on the Bloch's Theorem:

- For the periodic layout, the wave function is written as the combination of a cell periodic component and a wave-like component:

$$\psi(\gamma + \Delta\gamma) = \varphi(\gamma) \cdot \exp(jk\Delta\gamma)$$

- The equation above needs to have a pre-defined value for the k-vector; which is not so feasible for an FDTD simulation, especially for Pulse input.

Therefore, we simplified the application by setting the k-vector in one specific direction as zero, which then leads to the input wave being the axis-propagated wave, and then the equation becomes:

$$\psi\,(\gamma + \Delta\gamma) = \varphi(\gamma)$$

$\varphi(\gamma)$ is the field component at the edge of the simulation domain. $\psi\,(\gamma + \Delta\gamma)$ Is the corresponding field value at the boundary of the opposite edge of the $\varphi(\gamma)$. the following graph [18] shows the relationship.

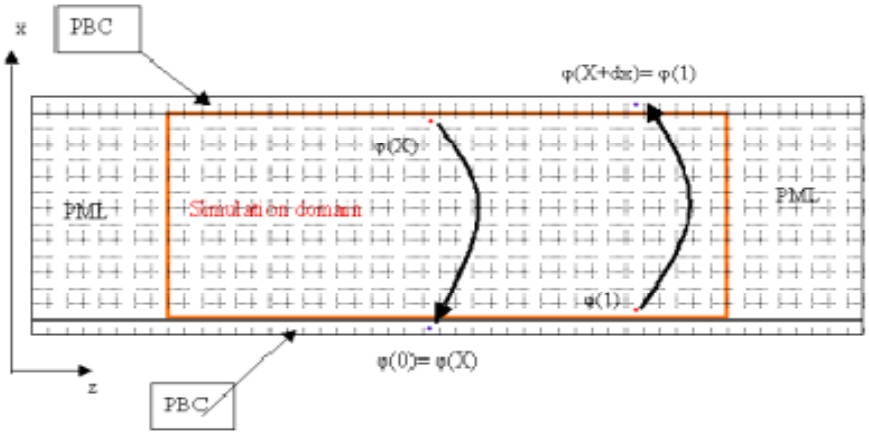

2.3 The Algorithm

Since the FDTD technique has been explained starting from the basics of technique to the boundary conditions. Now the FDTD algorithm can be defined that is be used in the modeling and simulations of the defined structures.

The finite difference time domain (FDTD) algorithm [19] is an especially popular tool because it is Simple, robust, and easy to understand. Here the FDTD algorithm has been explained by considering the Telegrapher's equations [20] which are in form of Partial differential equation in space and time.

The Telegrapher's Equations

The telegrapher's equations are basically nothing more than a pair of coupled partial differential equations (PDEs) in space and time. Together, they represent the fundamental governing equations of all transmission line theory [20], and are given as

$$-\frac{\partial v(z,t)}{\partial z} = R'i(z,t) + L'\frac{\partial i(z,t)}{\partial t}, \qquad (28)$$

$$-\frac{\partial i(z,t)}{\partial z} = G'v(z,t) + C'\frac{\partial v(z,t)}{\partial t}, \qquad (29)$$

Where v(z, t) and i(z ,t) represent the instantaneous voltage and current at position z and time t. The R', *L′*, *G′*, and *C* terms represent the resistance, inductance, conductance, and capacitance per unit length.

Because computers only have a finite capacity for memory storage, the first step in applying FDTD is to define a mesh, which is a set of discrete points in space and time that will sample our functions. Shown in figure 2(o), this is done by fixing a grid spacing of A_z in space and A_t in time. The points that lie on the mesh are then defined as

$$z_k = k\Delta z \qquad (30)$$

$$t_n = n\Delta t \qquad (31)$$

Where k and n are the integers confined by sets (1 < k < K) and *(1* < n < N).

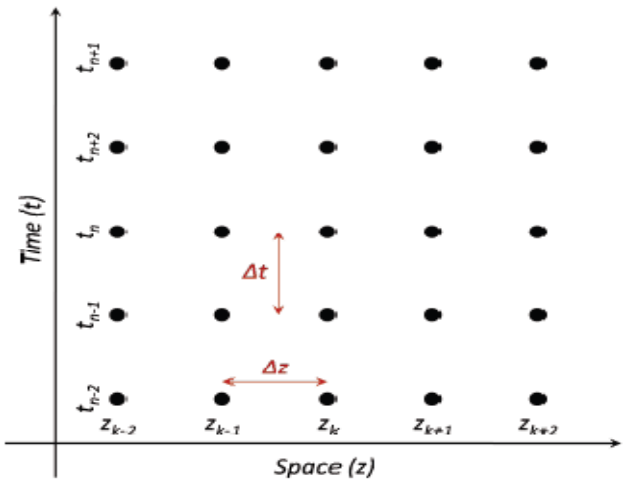

Figure 2(o). A simple FDTD mesh defined in space and time [20].

Now that the voltage and current functions have been sampled on a discrete, finite grid, we are ready to define a stencil, which is simply a numerical approximation for the derivative that uses neighboring points along the mesh. For example, the spatial derivative acting on the voltage function can be approximated through the use of *a* forward finite-difference:

$$\frac{\partial v(z,t)}{\partial z} \approx \frac{v(z+\Delta z,t)-v(z,t)}{\Delta z} \qquad (32)$$

At this point, it is convenient to introduce a more compact notation for the function v (z_k, t_n) by simply shortening it to v_k^n. In other words, the subscript index represents the spatial grid point, while the superscript index represents the temporal grid point. Using this notation, the numerical derivative is rewritten as

$$\frac{\partial}{\partial x} v_k^n \approx \frac{v_k^{n+1}-v_k^n}{\Delta z} \qquad (33)$$

Note that as long as the difference length A_z is very small, this approximation can provide us with reasonably accurate results. Nevertheless, we still would like to minimize the error from this approximation. It is therefore best to approximate all of our derivatives by using the central-difference method because it is more accurate than either forward or backwards-differences [21].We shall therefore impose the approximation

$$\frac{\partial}{\partial x} v_k^n \approx \frac{v_{k+1}^n - v_{k-1}^n}{2\Delta z} \qquad (34)$$

Similarly, we can apply the same approximation to the time-derivatives. For example, the time derivative on the current function i (z, t) can be rewritten as

$$\frac{\partial}{\partial t} i_k^n \approx \frac{i_k^{n+1} - i_k^{n-1}}{2\Delta t} \qquad (35)$$

Using these new expressions, we are now ready to transform the telegrapher's equations into a pair of coupled, finite-difference equations. In terms of our new stencil notation, this is written as

$$-\frac{v_{k+1}^n - v_{k-1}^n}{2\Delta z} = R' i_k^n + L' \frac{i_k^{n+1} - i_k^{n-1}}{2\Delta t} \qquad (36)$$

$$-\frac{i_{k+1}^n - i_{k-1}^n}{2\Delta z} = G' i_k^n + C' \frac{v_k^{n+1} - v_k^{n-1}}{2\Delta t} \qquad (37)$$

The voltage mesh is staggered from the current mesh in both space and time by the convention

$v_k^n = v_{k+1/2}^n$ and $i_k^n = i_{k+1/2}^n$. and is shown in figure 2(p) also.

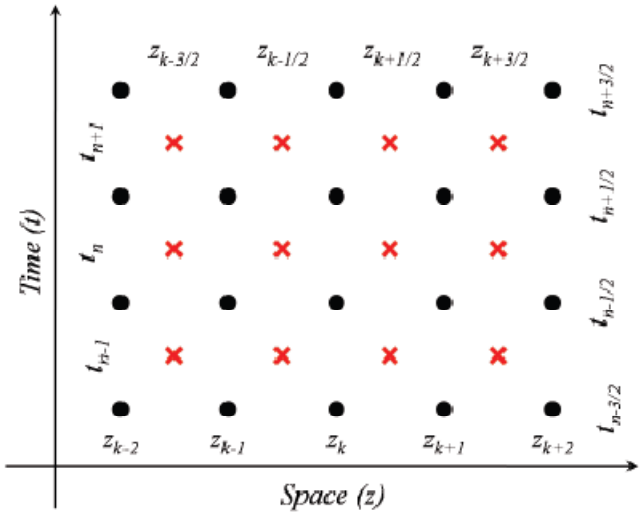

Figure 2(p): Revised FDTD mesh using the staggered grid [20].

The reason for redefining the meshes this way is so that we can approximate the spatial derivative on v as

$$\frac{\partial}{\partial t} v_k^n \approx \frac{v_{k+1/2}^n - v_{k-1/2}^n}{\Delta z} \qquad (38)$$

Similarly the temporal derivative on the current is approximated by centering on the nth time step using

$$\frac{\partial}{\partial t} i_k^n \approx \frac{i_k^{n+1} - i_k^{n-1}}{\Delta t} \qquad (39)$$

Applying these to (28) and (29) new set of finite difference equations becomes

$$\frac{v_{k+1/2}^n - v_{k-1/2}^n}{\Delta z} = R' i_k^n + L' \frac{i_k^{n+1/2} - i_k^{n-1/2}}{\Delta t} \qquad (40)$$

$$-\frac{i_{k+1}^{n+1/2}-i_{k}^{n-1/2}}{\Delta z}=G^{'}v_{k+1/2}^{n+1/2}+C^{'}\frac{v_{k+1/2}^{n+1}-v_{k+1/2}^{n}}{\Delta t} \quad (41)$$

Update Equations

The key concept behind the FDTD algorithm is to begin with some given "present" state for a system and then solve for the nearest "future" state. This is accomplished by taking the numerical telegrapher's equations and solving for the "future" terms.

$$i_{k}^{n+1/2}=c_1\left(v_{k+1/2}^{n}-v_{k-1/2}^{n}\right)+c_2\left(i_{k}^{n-1/2}\right) \quad (42)$$

and

$$v_{k+1/2}^{n+1}=c_3\left(i_{k+1}^{n+1/2}-i_{k}^{n+1/2}\right)+c_4\left(v_{k+1/2}^{n}\right) \quad (43)$$

Where

$$c_1=-\frac{2\Delta t}{\Delta t\Delta zR^{'}+2\Delta zL^{'}} \quad (44)$$

$$c_2=\frac{2L^{'}-\Delta tR^{'}}{2L^{'}+2\Delta tR^{'}} \quad (45)$$

$$c_3=-\frac{2\Delta t}{\Delta t\Delta zG^{'}+2\Delta zC^{'}} \quad (46)$$

$$c_4=\frac{2C^{'}-\Delta tG^{'}}{2C^{'}+\Delta tG^{'}} \quad (47)$$

The importance of equations (42) and (43) is that they provide a way to solve for the future state of the system in terms of surrounding points in space and time. A summary of the algorithm is provided as follows:

- Instantiate the samples of voltage and current over the simulation domain to their initial values.
- Loop over all values of k and solve for the future state of the current.
- Loop over all values of k and solve for future state of the voltage.

- Increment n.
- Process the new state of the system (ie, plot a graph, compute power flow, etc).
- If n is greater than the desired simulation time N, terminate the loop. Else, return to 2nd step.

This is the algorithm to initialize the FDTD grid given E and H at t=0 and then to update the grid till the defined time steps.

2.4 Plane Wave Expansion Method

The discovery of photonic crystals, periodic materials with photonic band gap, has opened up new methods for controlling light. In order to design photonic crystals to take advantage of their unique properties, a calculation method is necessary to determine how light will propagate through a particular crystal structure. Specifically, given any periodic dielectric structure, the allowable frequencies also known as eigen-frequencies or eigen -modes for light propagation in all crystal directions must be detected and the field distributions in the crystal for any frequency of light must be calculated. There are several capable techniques, but one of the most studied and reliable method is the plane wave expansion method. It was used in some of the earliest studies of photonic crystals and is simple enough to be easily implemented. The method allows the computation of eigen- frequencies for a photonic crystal to any prescribed accuracy, commensurate with computing time.

The plane wave expansion (PWE) method [22] is for the band structure calculations of the general periodic structures, where the structures extend periodically in all dimensions. Plane wave expansion method refers to a computational technique in electromagnetics to solve the Maxwell's equations by formulating an eigen value problem [23] out of the equation. This method is popular among the photonic crystal community as a method of solving for the band structure or the dispersion relation of specific photonic crystal geometries. PWE is traceable to the analytical formulations, and is useful in calculating modal solutions of Maxwell's equations over an inhomogeneous or periodic geometry. It is specifically tuned to solving problems in time-harmonic forms, with non-dispersive media.

The Maxwell equation in a transparent, time-invariant, source free and non-magnetic medium can be written in the following form:

$$\nabla \times \frac{1}{\varepsilon(\vec{r})} \nabla \times \vec{H}(\vec{r}) = \frac{\omega^2}{c^2} \vec{H}(\vec{r}) \qquad (48)$$

Where $\varepsilon(\vec{r})$the space dependent dielectric function, c is is speed of light in vacuum and $\vec{H}(\vec{r})$is the optical magnetic field vector of a definite frequency ω with time dependence e^{iwt}. This equation is sometimes called master equation [23] and represents a Hermitian Eigen problem [23] which could not be said if the wave equation were derived in terms of the electric field.

The Bloch theorem [24] says that due to the infinite periodicity, the magnetic field will take a form of

$$\vec{H}(\vec{r}) = e^{i\vec{k}\vec{r}} \vec{h}_k(\vec{r}), \qquad (49)$$

Where $\vec{h}(\vec{r}) = \vec{h}(\vec{r} + \vec{R})$for all combinations of lattice vectors $\vec{R}$. Thus we end up with the master equation in operator form:

$$(\nabla + i\vec{k}) \times \left\{ \frac{1}{\varepsilon(\vec{r})} (\nabla + i\vec{k}) \right\} \times \vec{h}_k = \frac{\omega^2}{c^2} \vec{h}_k \qquad (50)$$

This is the fundamental equation, which needs to be solved. The equation is transformed into a finite problem by expanding the magnetic field in a finite basis of simple plane waves. Different approaches can be explored to solve the final discretized problem. The result of solving the discretized problem is the dispersion relationship between the frequencies of the modes and wave vector $\overrightarrow{R}$, usually plotted in the form of a band diagram.

PWE expansions are rigorous solutions. PWE is extremely well suited to the modal solution problem. Large size problems can be solved using iterative techniques. For both generalized and normal eigen value problems, just a few band-index plots in the band-structure diagrams are required, usually lying on the brillouin zone edges [24]. This corresponds to eigen modes solutions using iterative techniques, as opposed to diagonalization of the entire matrix.

Though plane wave method is quite successful in photonic band gap calculations, it has several limitations. The computation grows exponentially when the problem size increases.

For complicated problems, such as three dimensional photonic band gap calculations, the computation is intensive. A less computationally intensive eigen solver is critical to reduce computation effectively.

CHAPTER 3 PHOTONIC CRYSTALS AND MATERIALS

3.1 Introduction

Many of the true breakthroughs in our technology have resulted from a deeper understanding of the properties of materials. The rise of our ancestors from the Stone Age through the Iron Age is largely a story of humanity's increasing recognition of the utility of natural materials. Prehistoric people fashioned tools based on their knowledge of the durability of stone and the hardness of iron. In each case, humankind learned to extract a material from the Earth whose fixed properties proved useful. Eventually, early engineers learned to do more than just take what the Earth provides in raw form. By tinkering with existing materials, they produced substances with even more desirable properties, from the luster of early bronze alloys to the reliability of modern steel and concrete. Today we boast a collection of wholly artificial materials with a tremendous range of mechanical properties, thanks to advances in metallurgy, ceramics, and plastics.

In this century, our control over materials has spread to include their electrical properties. Advances in semiconductor physics have allowed us to tailor the conducting properties of certain materials, thereby initiating the transistor revolution in electronics. It is hard to overstate the impact that the advances in these fields have had on our society. With new alloys and ceramics, scientists have invented high-temperature superconductors and other exotic materials that may form the basis of future technologies. In the last few decades, a new frontier has opened up. The goal in this case is to control the optical properties of materials. An enormous range of technological developments would become possible if we could engineer materials that respond to light waves over a desired range of frequencies by perfectly reflecting them, or allowing them to propagate only in certain directions, or confining them within a specified volume. Already, fiber-optic cables, which simply guide

light, have revolutionized the telecommunications industry. Laser engineering, high-speed computing, and spectroscopy are just a few of the fields next in line to reap the benefits from the advances in optical materials.

What sort of material can afford us complete control over light propagation? To answer this question, we rely on an analogy with our successful electronic materials. A crystal is a periodic arrangement of atoms or molecules. The pattern with which the atoms or molecules are repeated in space is the crystal **lattice**. The crystal presents a periodic potential to an electron propagating through it, and both the constituents of the crystal and the geometry of the lattice dictate the conduction properties of the crystal.

The theory of quantum mechanics in a periodic potential explains what was once a great mystery of physics: In a conducting crystal, why do electrons propagate like a diffuse gas of free particles? How do they avoid scattering from the constituents of the crystal lattice? The answer is that electrons propagate as waves, and waves that meet certain criteria can travel through a periodic potential without scattering (although they will be scattered by defects and impurities).

Importantly, however, the lattice can also prohibit the propagation of certain waves. There may be **gaps** in the energy band structure of the crystal, meaning that electrons are forbidden to propagate with certain energies in certain directions. If the lattice potential is strong enough, the gap can extend to cover all possible propagation directions, resulting in a **complete band gap**. For example, a semiconductor has a complete band gap between the valence and conduction energy bands. The optical analogue is the photonic crystal, in which the atoms or molecules are replaced by macroscopic media with differing dielectric constants, and the periodic potential is replaced by a periodic dielectric function (or, equivalently, a periodic index of refraction). If the dielectric constants of the materials in the crystal are sufficiently different, and if the absorption of light by the materials is minimal, then the refractions and reflections of light from all of the various interfaces can produce many of the same phenomena for photons (light modes) that the atomic potential produces for electrons. One solution to the problem of optical control and manipulation is thus a **photonic crystal**, a low-loss periodic dielectric medium. In particular, we can design and

construct photonic crystals with **photonic band gaps**, preventing light from propagating in certain directions with specified frequencies (i.e., a certain range of wavelengths, or "colors," of light).We will also see that a photonic crystal can allow propagation in anomalous and useful ways.

To develop this concept further, consider how metallic waveguides and cavities relate to photonic crystals. Metallic waveguides and cavities are widely used to control microwave propagation. The walls of a metallic cavity prohibit the propagation of electromagnetic waves with frequencies below a certain threshold frequency, and a metallic waveguide allows propagation only along its axis. It would be extremely useful to have these same capabilities for electromagnetic waves with frequencies outside the microwave regime, such as visible light.

However, visible light energy is quickly dissipated within metallic components, which makes this method of optical control impossible to generalize. Photonic crystals allow the useful properties of cavities and waveguides to be generalized and scaled to encompass a wider range of frequencies. We may construct a photonic crystal of a given geometry with millimeter dimensions for microwave control, or with micron dimensions for infrared control.

Another widely used optical device is a multilayer dielectric mirror, such as a quarter-wave stack, consisting of alternating layers of material with different dielectric constants. Light of the proper wavelength, when incident on such a layered material, is completely reflected. The reason is that the light wave is partially reflected at each layer interface and, if the spacing is periodic, the multiple reflections of the incident wave interfere destructively to eliminate the forward-propagating wave. This well-known phenomenon, first explained by Lord Rayleigh in 1887, is the basis of many devices, including dielectric mirrors, dielectric Fabry–Perot filters, and distributed feedback lasers. All contain low-loss dielectrics that are periodic in one dimension, and by our definition they are one dimensional photonic crystal. Even these simplest of photonic crystals can have surprising properties. We will see that layered media can be designed to reflect light that is incident from any angle, with any polarization—an

omnidirectional reflector—despite the common intuition that reflection can be arranged only for near-normal incidence.

If, for some frequency range, a photonic crystal prohibits the propagation of electromagnetic waves of any polarization traveling in any direction from any source, we say that the crystal has a **complete photonic band gap**. A crystal with a complete band gap will obviously be an omnidirectional reflector, but the converse is not necessarily true. As we shall see, the layered dielectric medium mentioned above, which cannot have a complete gap (because material interfaces occur only along one axis), can still be designed to exhibit omnidirectional reflection—but only for light sources far from the crystal.

Usually, in order to create a complete photonic band gap, one must arrange for the dielectric lattice to be periodic along three axes, constituting a three-dimensional photonic crystal. However, there are exceptions. A small amount of disorder in an otherwise periodic medium will not destroy a band gap (Fan et al., 1995b; Rodriguez et al., 2005), and even a highly disordered medium can prevent propagation in a useful way through the mechanism of **Anderson localization** (John, 1984). Another interesting nonperiodic class of materials that can have complete photonic band gaps is quasi-crystalline structures (Chan et al., 1998).

3.2 One-Dimensional Photonic Crystal

We begin our study of photonic crystals by considering the simplest possible case, a one-dimensional system, and applying the principles of electromagnetism and symmetry that we developed in the previous chapters. Even in this simple system, we can discern some of the most important features of photonic crystals in general, such as photonic band gaps and modes that are localized around defects. The optical properties of a one-dimensional layered system may be familiar, but by expressing the results in the language of band structures and band gaps, we can discover new phenomena such as omnidirectional reflectivity, as well as prepare for the more complicated two- and three-dimensional systems that lie ahead.

The simplest possible photonic crystal, shown in figure 1, consists of alternating layers of material with different dielectric constants: a **multilayer film**. This arrangement is not a new idea. Lord Rayleigh (1887) published one of the first analyses of the optical properties of

multilayer films. As we will see, this type of photonic crystal can act as a mirror (a **Bragg mirror**) for light with a frequency within a specified range, and it can localize light modes if there are any defects in its structure. These concepts are commonly used in dielectric mirrors and optical filters (as in, e.g., Hecht and Zajac, 1997).

The traditional way to analyze this system, pioneered by Lord Rayleigh (1917), is to imagine that a plane wave propagates through the material and to consider the sum of the multiple reflections and refractions that occur at each interface. In this chapter, we will use a different approach—the analysis of band structures—that is easily generalized to the more complex two- and three dimensional photonic crystals.

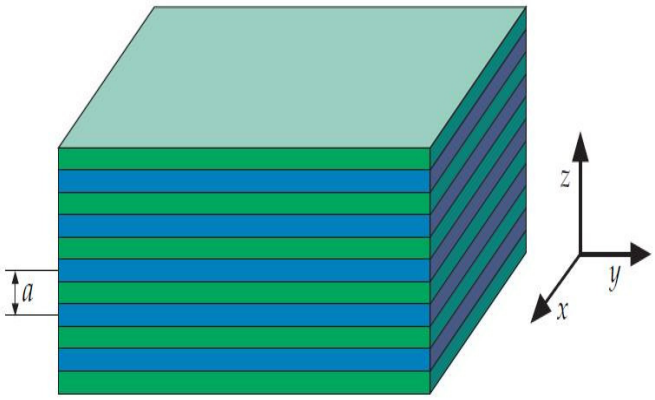

Figure 3(a): 1D photonic crystal

3.3 Two-dimensional photonic crystals

In two dimensions, holes may be drilled in a substrate that is transparent to the wavelength of radiation that the bandgap is designed to block. Triangular and square latices of holes have been successfully employed.

The Holey fiber or photonic crystal fiber can be made by taking cylindrical rods of glass in hexagonal lattice, and then heating and stretching them, the triangle-like airgaps between the glass rods become the holes that confine the modes.

A two-dimensional photonic crystal is periodic along two of its axes and homogeneous along the third axis. A typical specimen, consisting of a square lattice of dielectric columns, is

shown in figure. We imagine the columns to be infinitely tall; the case of a finite extent in the third direction is treated in chapter 8. For certain values of the column spacing, this crystal can have a photonic band gap in the xy plane. Inside this gap, no extended states are permitted, and incident light is reflected. Unlike the multilayer film, this two-dimensional photonic crystal can prevent light from propagating in any direction within the plane.

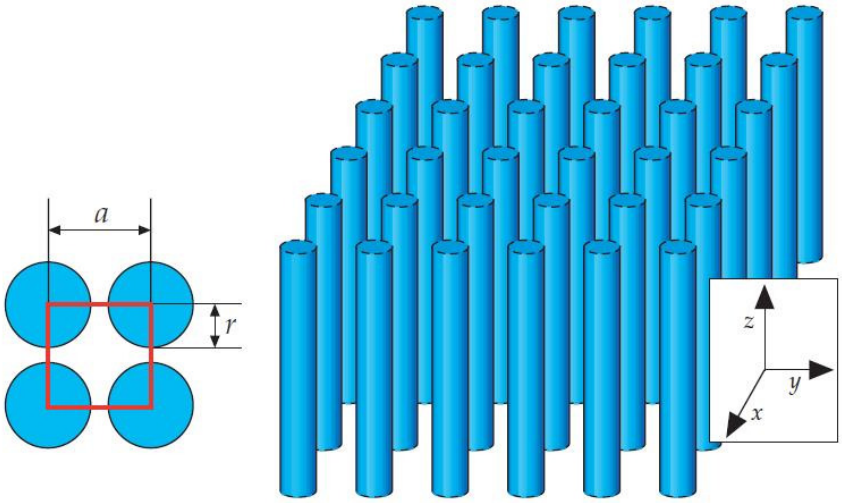

Figure 3(b): 2D photonic crystal

This material is a square lattice of dielectric columns, with radius r and dielectric constant ε. The material is homogeneous along the z direction (we imagine the cylinders are very tall), and periodic along x and y with lattice constant a.

3.4 Three-dimensional photonic crystals

THE OPTICAL ANALOGUE of an ordinary crystal is a three-dimensional photonic crystal: a dielectric structure that is periodic along three different axes. Three dimensional photonic crystals can have the novel properties we discussed in the previous two chapters, including band gaps, defect modes, and surface states. Just as in two dimensions, we can localize light at a defect or at a surface, but with a three-dimensional crystal we have the additional capability to localize light in all three dimensions.

There are several structure types that have been constructed:

- Spheres in a diamond lattice

- Yablonovite

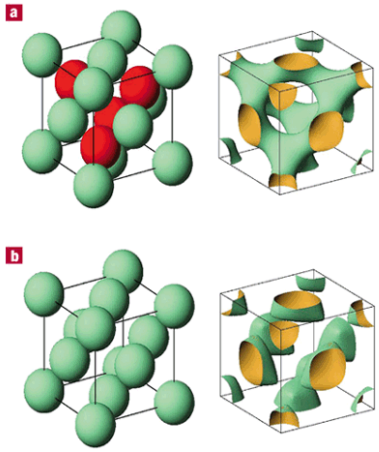

Figure 3(c): 3D photonic crystal (Yablonovite).

- The Woodpile Structure – "rods" are repeatedly etched using beam lithography, filled in and new material is then deposited thereon, and the process is repeated on the next layer with etched channels that are perpendicular to the layer below, and parallel to and out of phase with the channels two layers below. The process is repeated until the structure is of the desired height. The fill-in material is then dissolved using an agent that can dissolve the fill in material but not the deposition material. It is generally hard to introduce defects into this structure.
- Inverse opals or Inverse Colloidal Crystals-Spheres (such as polystyrene) can be allowed to deposit into a cubic close packed lattice suspended in a solvent. Then a hardener is introduced which makes a transparent solid out of the volume occupied by the solvent. The spheres are then dissolved using an acid such as Hydrochloric acid.
- A stack of two-dimensional crystals - This is a more general class of photonic crystals than Yablonivite, but the original implementation of Yablonovite was created using this method.

3.5 Recent work

Until recently, an optical fiber was a solid thread surrounded by another material with a lower refractive index. Today the photonic crystal fibers (PCFs) are established as an alternative fiber technology. PCFs, which have been first demonstrated in 1995, are optical fibers with a periodic arrangement of low-index material in a background with higher

refractive index. The background material in PCFs is usually undoped silica and the low-index region is typically provided by air-holes running along their entire length. Two main categories of PCFs exist: high-index guiding fibers and photonic bandgap ones. PCFs belonging to the first category are more similar to conventional optical fibers, because light is confined in a solid core by exploiting the modified total internal reflection mechanism. In fact, there is a positive refractive index difference between the core region and the photonic crystal cladding, where the air-hole presence causes a lower average refractive index. The guiding mechanism is defined as "modified" because the cladding refractive index is not a constant value as in standard optical fibers but it changes significantly with the wavelength. This characteristic as well as the high refractive index contrast between silica and air provides a range of new interesting features. Moreover, high design flexibility is one of the distinctive properties of PCFs. In particular, by changing the geometric characteristics of the air-holes in the fiber cross-section, that is, their dimension or position, it is possible to obtain PCFs with diametrically opposite properties. For example, PCFs with a small silica core and large air-holes, that is, with a high air-filling fraction in the transverse section have better nonlinear properties compared with conventional optical fibers and so they can be successfully used in many applications, like supercontinuum generation.

On the contrary fibers can be designed with small air-holes and large hole-to-hole distances in order to obtain a large modal area, useful for high power delivery. Differently from standard fibers PCFs with proper geometric characteristics can be endlessly single mode, that is, only the fundamental mode is guided regardless of the wavelength. In addition a significant asymmetry can be introduced in a simple way in the PCF core, thus creating fibers with very high level of birefringence. Moreover the PCF dispersion properties can be tailored with high flexibility so that it is possible to move the zero-dispersion wavelength to the visible range as well as to obtain dispersion curves ultra flattened or with a strong negative slope.

When the PCF core region has a lower refractive index than the surrounding photonic crystal cladding, light is guided by a mechanism different from total internal reflection - by exploiting the presence of the photonic bandgap (PBG). In fact, the air-hole microstructure which constitutes the PCF cladding is a two-dimensional photonic crystal that is a material

with periodic dielectric properties characterized by a photonic bandgap, where light in certain wavelength ranges cannot propagate. The PBG effect can be also found in nature since it is responsible, for example, of the beautiful and bright colors seen in butterfly wings. PCFs with a low index core are created by introducing a defect in the photonic crystal structure, for example, an extra air-hole or an enlarged one, and light is confined because the PBG makes propagation in the micro structured cladding region impossible. This guiding mechanism cannot be obtained in conventional optical fibers and it opens a whole new set of interesting possibilities. In particular, light can be guided in air in PCFs with a hollow core thus providing numerous promising applications such as low-loss guidance and high-power delivery without the risk of fiber damage. Moreover air-guiding PCFs are almost insensitive to bending even for small bending diameter values and they present extreme dispersion properties, highly dominated by the waveguide component. Finally, when filled with proper gases or liquids, hollow core PCFs can be successfully employed in sensor applications or for nonlinear optics.

Since their first demonstration, PCFs have been the object of an intense research activity by the most important groups all around the world. In fact, it is particularly intriguing to study the new light-guiding mechanisms offered by PCFs and the innovative properties related to the presence of the PBG. Moreover, the possibility of modifying the air-hole geometry in the fiber cross-section is limited only by the technological feasibility of the designed PCFs. It is also very interesting to investigate how the PCF properties can be influenced by the changes of the geometric characteristics and how far it is possible to go from the well-known and established properties of standard optical fibers.

One of the most important advantages offered by photonic crystal fibers (PCFs) is the high design flexibility. In fact, by changing the geometric characteristics of the fiber cross-section such as the air-hole dimension or disposition, it is possible to obtain fibers with diametrically opposed optical properties. PCFs with unusual guiding, dispersion and nonlinear properties can be designed and successfully used in various applications as reported in this section.

The main drawback which affects this new kind of fibers is related to the attenuation, which is higher than that of conventional optical fibers. The different loss mechanisms are thus

analyzed for both solid- and hollow-core photonic crystal fibers. In general, a loss reduction for PCFs can be obtained by improving the fabrication process, reported in the last part of the chapter. The stack-and draw process is described with other fabrication techniques [25]. Once reached the technological maturity, the advantages offered by PCFs with respect to conventional fibers could be completely exploited for different applications [25] and the new fibers will enter concretely in the market.

3.6 Optical Fibers to Photonic Crystal Fibers

Optical fibers which transmit information in the form of short optical pulses over long distances at exceptionally high speeds are one of the major technological successes of the 20th century. This technology has developed at an incredible rate, from the first low-loss single-mode waveguides in 1970 to being key components of the sophisticated global telecommunication network. Optical fibers have also non-telecom applications like the ion beam delivery for medicine, machining and diagnostics, sensing and a lot of other fields. Modern optical fibers represent a careful trade-off between optical losses, optical nonlinearity, group velocity, and dispersion and polarization effects. After 30 years of intensive research, incremental steps have refined the capabilities of the system and the fabrication technology nearly as far as they can go. The interest of researchers and engineers in several laboratories since the 1980s has been attracted by the ability to structure materials on the scale of the optical wavelength, a fraction of micrometers or less, in order to develop new optical medium known as photonic crystals. Photonic crystals rely on a regular morphological microstructure, incorporated into the material, which radically alters its optical properties. They represent the extension of the results obtained for semiconductors into optics. In fact the band structure of semiconductors is the outcome of the interactions between electrons and the periodic variations in potential created by the crystal lattice. By solving the Schrodinger's wave equation for a periodic potential electron energy states separated by forbidden bands are obtained. PBGs can be obtained in photonic crystals where periodic variations in dielectric constant, that is in refractive index, substitute variations in electric potential as well as the classical wave equation for the magnetic field replaces the Schrodinger's equation [25]. PBG originally predicted in 1987 by Sajeev John from University of Toronto and Eli Yablonovitch from Bell Communications Research has become the really hot topic in optics in the early 1990s. The idea was to build the right

structures, in order to selectively block the transmission of photons with energy levels that is wavelengths corresponding to the PBGs while allowing other wavelengths to pass freely. Moreover slight variations in the refractive index periodicity would introduce new energy levels within the PBG as it happens with the creation of energy levels within the bandgap of conventional semiconductors. Unfortunately, building the right structures has proved extremely difficult. The first PBG material was created in 1991 by Yablonovitch and his colleagues by drilling holes with a diameter of 1mm in a block of material with a refractive index of 3.6. Since the bandgap wavelength is of the order of the spacing between the air-holes in the photonic crystal, this structure had a bandgap in the microwave region. In 1991, Philip Russell [25] who was interested in Yablonovitch's research got his big "crazy" idea for "something different" .Russell's idea was that light could be trapped inside a fiber hollow core by creating a two-dimensional photonic crystal in the cladding that is a periodic wavelength scale lattice of microscopic air-holes in the glass. The basic principle is the same which is the origin of the color in butterfly wings and peacock feathers, that is all wavelength scale periodic structures exhibit ranges of angle and color, stop bands where incident light is strongly reflected. When properly designed the photonic crystal cladding running along the entire fiber length can prevent the escape of light from the hollow core. These new fibers are called PCFs, since they rely on the unusual properties of photonic crystals. The first fiber with a photonic crystal structure was reported by Russell and his colleagues in 1996. Even if it was a very interesting research development, the first PCF did not have a hollow core as shown in Fig. 3(d) and consequently it did not rely on a photonic bandgap for optical confinement. In fact, in 1996 Russell's group could produce fiber with the necessary air-hole triangular lattice but the air-holes were too small to achieve a large air-filling fraction which is fundamental to realize a PBG. Measurements have shown that this solid-core fiber formed a single-mode waveguide that is only the fundamental mode was transmitted over a wide wavelength range. Moreover the first PCF had very low intrinsic losses due to the absence of doping elements in the core and a silica core with an area about ten times larger than that of a conventional single mode fiber (SMF), thus permitting a corresponding increase in optical power levels.

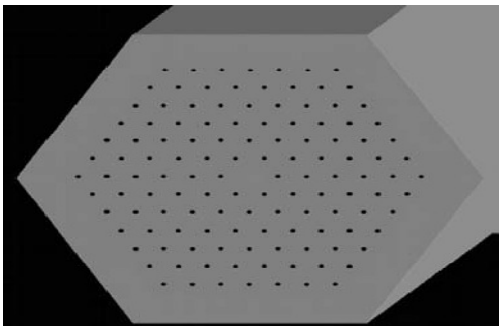

Figure 3(d): Schematic of the cross-section of the first solid-core photonic crystal fiber with air hole diameter of 300 nm and hole-to-hole spacing of 2.3 μm [25].

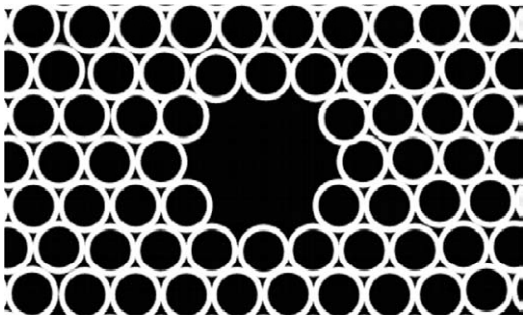

Figure 3(e): Schematic of the cross-section of the first hollow-core PCF, with hole-to-hole spacing of 4.9 μm and core diameter of 14.8 μm [25].

After moving his research group to the University of Bath where PCF fabrication techniques were steadily refined, Russell and his co-workers were able to report the first single mode hollow-core fiber in which confinement was due by a full two-dimensional PBG as reported in Fig. 3(e). They realized that the photonic bandgap guiding mechanism is very robust since light remains well confined in the hollow core even if tight bends are formed in the fiber. Initial production techniques were directed simply at the task of making relatively short lengths of fiber in order to do the basic science but many research teams are now working hard to optimize their PCF production techniques in order to increase the lengths and to reduce the losses.

3.7 Wave propagation mechanism

In order to form a guided mode in an optical fiber, it is necessary to introduce light into the core with a value of β that is the component of the propagation constant along the fiber axis,

which cannot propagate in the cladding. The highest β value that can exist in an infinite homogeneous medium with refractive index n is $\beta = nk_0$, being k_0 the free-space propagation constant. All the smaller values of β are allowed. A two-dimensional photonic crystal like any other material is characterized by a maximum value of β which can propagate. At a particular wavelength, this corresponds to the fundamental mode of an infinite slab of the material and this β value defines the effective refractive index of the material.

Modified Total Internal Reflection

It is possible to use a two-dimensional photonic crystal as a fiber cladding by choosing a core material with a higher refractive index than the cladding effective index. An example of this kind of structures is the PCF with a silica solid core surrounded by a photonic crystal cladding with a triangular lattice of air-holes, shown in Fig. 3(f). These fibers also known as index-guiding PCFs guide light through a form of total internal reflection (TIR) called modified TIR. However they have many different properties with respect to conventional optical fibers.

Endlessly single-mode property

As already stated, the first solid-core PCF shown in Fig. 3(d), which consisted of a triangular lattice of air-holes did not ever seem to become multi-mode in the experiments even for short wavelengths. In fact, the guided mode always had a single central lobe filling the core [26].

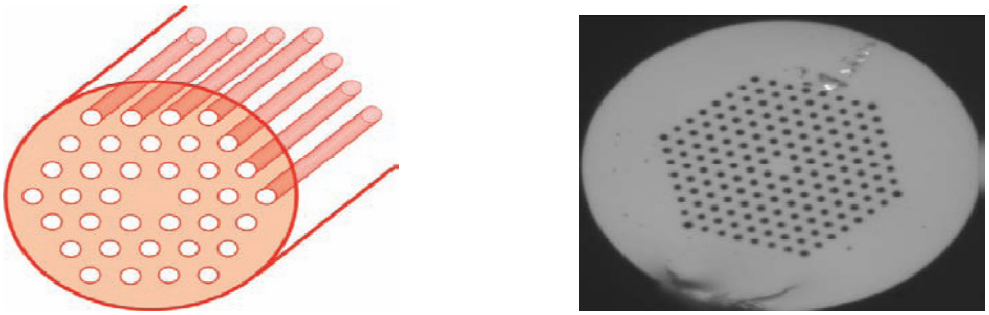

(i) (ii)

Figure 3(f): (i) Schematic of a solid-core PCF with a triangular lattice of air-holes, which guides light for modified total internal reflection. (ii) Microscope picture of a fabricated solid-core triangular PCF [26]

Russell has explained that this particular endlessly single-mode behavior can be understood by viewing the air-hole lattice as a modal filter or sieve [26]. A proper geometry design of the fiber cross-section thus guarantees that only the fundamental mode is guided. By exploiting this property, it is possible to design very large-mode area fibers which can be successfully employed for high power delivery, amplifiers and lasers. Moreover by doping the core in order to slightly reduce its refractive index light guiding can be turned off completely at wavelengths shorter than a certain threshold value.

Photonic Bandgap Wave Propagation

Optical fiber designs completely different form the traditional ones result from the fact that the photonic crystal cladding have gaps in the ranges of the supported modal index β/k_0 where there are no propagating modes. These are the PBGs of the crystal which are similar to the two-dimensional band gaps which characterize planar light wave circuits, but in this case they have propagation with a non-zero value of β. It is important to underline that gaps can appear for values of modal index both greater and smaller than unity, enabling the formation of hollow-core fibers with bandgap material as a cladding, as reported in Fig. 3(g).

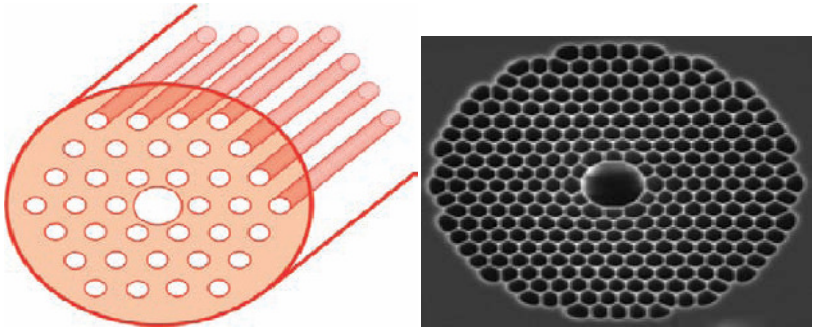

(i) (ii)

Figure 3(g): (i) Schematic of a hollow-core PCF with a triangular lattice of air-holes, which guides light through the photonic bandgap effect. (ii) Microscope picture of a fabricated hollow-core triangular PCF [26].

These fibers which cannot be made using conventional optics are related to Bragg fibers, since they do not rely on TIR to guide light. In fact, in order to guide light by TIR it is necessary a lower-index cladding material surrounding the core but there are no suitable low-loss materials with a refractive index lower than air at optical frequencies. The first PCF

which exploited the PBG effect to guide light was reported in 1998 [27] and it is shown in Figure 3(g). Notice that its core is formed by an additional air-hole in a honeycomb lattice. This PCF could only guide light in silica, the higher-index material.

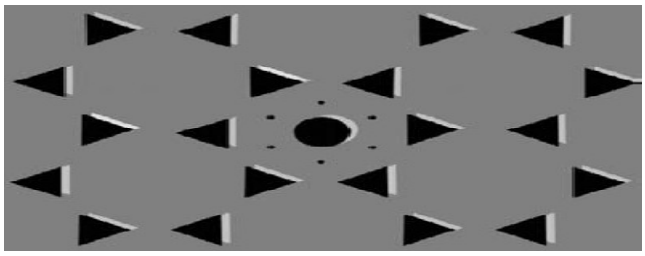

Figure 3(h): Schematic of the cross-section of the first photonic bandgap PCF with a honeycomb air-hole lattice [27].

Hollow-core guidance had to wait until 1999 when the PCF fabrication technology had advanced to the point where larger air-filling fractions required achieving PBG for air-guiding became possible. Notice that an air guided mode must have $\beta/k_0 < 1$, since this condition guarantees that light is free to propagate and form a mode within the hollow core, while being unable to escape into the cladding. The first hollow-core PCF reported in Figure 3(e) had a simple triangular lattice of air-holes and the core was formed by removing seven capillaries in the center of the fiber cross-section. By producing a relatively large core, the chances of finding a guided mode were improved. When white light is launched into the fiber core colored modes are transmitted, thus indicating that light guiding exists only in restricted wavelength ranges which coincide with the photonic band gaps [27].

3.6 Loss mechanisms

The most important factor for any optical fiber technology is loss. Losses in conventional optical fibers have been reduced over the last 30 years and a further improvement is unlikely to be reached. The minimum loss in fused silica which is around 1550nm, is slightly less than 0.2 dB/km. This limit is important since it sets the amplifier spacing in long-haul communications systems, and thus is a major cost of a long-haul transmission system. Loss mechanisms in PCFs are here described in details, in order to understand how far the technology can go to reduce their values.

Intrinsic loss

In Solid-core fibers the optical loss α_{dB}, measured in dB/km, of PCFs with a sufficiently reduced confinement loss, which can be expressed as

$$\alpha_{dB} = A/\lambda 4 + B + \alpha_{OH} + \alpha_{IR} \qquad (1)$$

being A, B, α_{OH}, and α_{IR} the Rayleigh scattering coefficient, the imperfection loss, and OH and infrared absorption losses, respectively. At the present time the losses in PCFs are dominated by OH-absorption loss and imperfection loss [30].

In a typical PCF the OH-absorption loss is more than 10dB/km at 1380 nm and this causes an additional optical loss of 0.1dB/km in the wavelength range around 1550 nm. Since this contribution is very similar to the intrinsic optical loss of 0.14dB/km for pure silica glass at this wavelength, the OH-absorption loss reduction becomes a challenging problem. Most of the OH impurities seem to penetrate the PCF core region during the fabrication process. As a consequence, a dehydration process is useful in reducing the OH-absorption loss [30].

Imperfection loss, caused mainly by air-hole surface roughness is another serious problem. In fact, during the fabrication process the air-hole surfaces can be affected by small scratches and contamination. If this surface roughness is comparable with the considered wavelength, it can significantly increase the scattering loss. Thus it is necessary to improve the polishing and etching process in order to reduce the optical loss caused by this roughness. Moreover fluctuation in the fiber diameter during the fiber drawing process can cause an additional imperfection loss if the air-hole size and pitch change along the fiber [30].

It is important to underline that the Rayleigh scattering coefficient of PCFs is the same as that of a conventional SMF. However this is higher than that of a pure silica-core fiber, although the PCF is made of pure silica glass. It is necessary to reduce the roughness further, in order to obtain a lower imperfection loss and a lower Rayleigh scattering coefficient. It is fundamental to fabricate long PCFs with low loss, if they are to be used as transmission media.

In Fig. 3(m), the decrease of the loss for fabricated index-guiding PCFs is shown until 2006. Early in their development, solid-core PCFs had optical losses of the order of 0.24dB/m [31] and the available length was limited to several meters. The optical losses of PCFs were rapidly reduced to 1 dB/km by improving the fabrication process [31]. The lowest loss yet achieved is 0.28dB/km [31]. Recently a low loss that is 0.3dB/km, and long length, that is 100 km, PCF was reported [31].

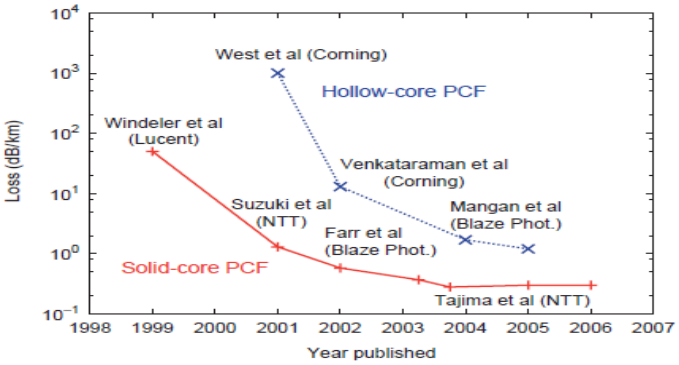

Figure 3(m): Optical loss behavior during the last years, until 2006, for solid core (+ symbols) and hollow-core (× symbols) PCFs [30].

The optical losses of these kinds of PCFs are still high compared with those of a conventional SMF. However, a solid-core PCF is not expected to have significantly lower losses than standard fibers.

Losses in hollow-core fibers are limited by the same mechanisms as in conventional fibers and in index-guiding PCFs, that are absorption, Rayleigh scattering, confinement loss, bend loss, and variations in the fiber structure along the length. However, there is the possibility to reduce them below the levels found in conventional optical fibers since the majority of the light travels in the hollow core, in which scattering and absorption could be very low.

As shown in Fig. 3(m), the attenuation values reported in literature for hollow-core PCFs are higher than those for both solid-core PCFs and standard fibers. Looking at the attenuation profiles for a range of hollow-core fibers made by Crystal Fibre, it is possible to notice two important facts. The guiding bandwidth is usually around 15% of the central wavelength and the loss scales inversely with the wavelength. As indicated by theoretical considerations, the

attenuation related to mode coupling and scattering at the internal air silica interfaces scale with the wavelength. This consideration has been confirmed by experimental observations [31] and applies to the seven-cell design, whose hollow core has been obtained by removing seven capillaries in the center of the fiber cross-section.

It is important to underline that, in order to reach lower losses, 19-cell designs can be used, as it is demonstrated by the loss values reported in Fig. 3(n). The minimum loss of 1.7 dB/km has been obtained with the hollow-core PCF [31] shown in Fig. 3(o), since the larger core reduces the overlap of the guided modes with silica.

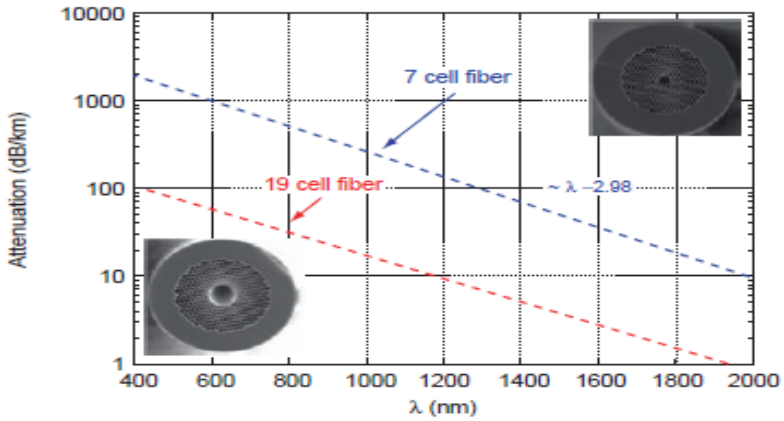

Figure 3(n): Attenuation behavior versus the wavelength for 7-cell and 19- cell hollow-core PCFs, whose cross-sections are shown as inset [31].

However notice that a larger hollow core gives increased perimeters, leading to a greater density of surface modes, decreased bandwidth and also to increased higher-order dispersion [31]. Reducing the hollow-core PCF loss to levels below those of conventional silica fibers remains a challenge. For what concerns Rayleigh scattering as well as absorption, they should be reduced to below the level in bulk fibers, even if the increased scattering at the many surfaces represents potentially a problem.

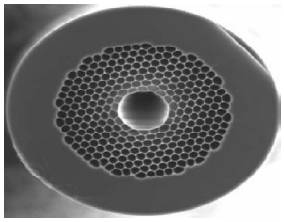

Figure 3(o): Microscope picture of a 19-cell hollow-core fiber [31]

However, the biggest unknown is the level of variation in the fiber structure along its length. In fact, the band gap presents a high sensitivity to structural fluctuations that occur over long fiber lengths that is wavelengths that are guided in one section may leak away in another.

Finally, there is an excess loss in hollow-core PCFs which occurs at wavelengths where there is coupling from the air-guided fundamental mode to the confined surface modes, which have much greater overlap with the glass and, as a consequence, experience far higher loss. The presence of surface modes strongly affects the guiding properties of the air-guiding PCFs by reducing the width of their transmission window. Ideally, being the core modes completely confined in air, the small perturbations in the silica structure cause only a slight coupling with the cladding ones, which have the largest spatial overlap in the perturbed region [31].

A reduction of the silica quantity around the hollow core causes an energy increase of the surface modes which consequently move into the PBG while on the contrary the guided-mode energy is unaffected by this change. However for some hollow core dimensions there is a certain interaction between these two different kinds of modes, due to the significant field overlap in the silica regions. Thus, the axial perturbations all along the fiber can provide the light coupling between the core and the surface modes. The loss mechanism related to surface modes is complete by considering that they are highly overlapped and coupled with the continuum of the extended modes in the cladding.

Confinement Loss

In both solid-core and hollow-core PCFs it is necessary to consider another contribution to the losses, that is the leakage or confinement losses. These are due to the finite number of air-holes which can be made in the fiber cross section. As a consequence all the PCF guided modes are leaky. For example, in solid-core PCFs light is confined within a core region by the air-holes. Light will move away from the core if the confinement provided by the air-holes is inadequate. This means that it is important to design such aspects of the PCF structure as air-hole diameter and hole-to-hole spacing or pitch in order to realize low-loss PCFs. In particular, the ratio between the air-hole diameter and the pitch must be designed to be large enough to confine light into the core. On the other hand, a large value of the ratio

makes the PCF multi-mode. However by properly designing the structure the confinement loss of single-mode PCFs can be reduced to a negligible level.

Recently, several analyses have been performed in order to find the guidelines to design both index-guiding PCFs and PBG-based fibers with negligible leakage losses [32]. In particular leakage losses can be significantly reduced by increasing the ring number [32]. In PBG fibers the leakage loss dependence on the number of air-hole rings is much weaker than in index-guiding PCFs, whereas the confinement losses exhibit a strong dependence on the position of the localized state inside the PBG.

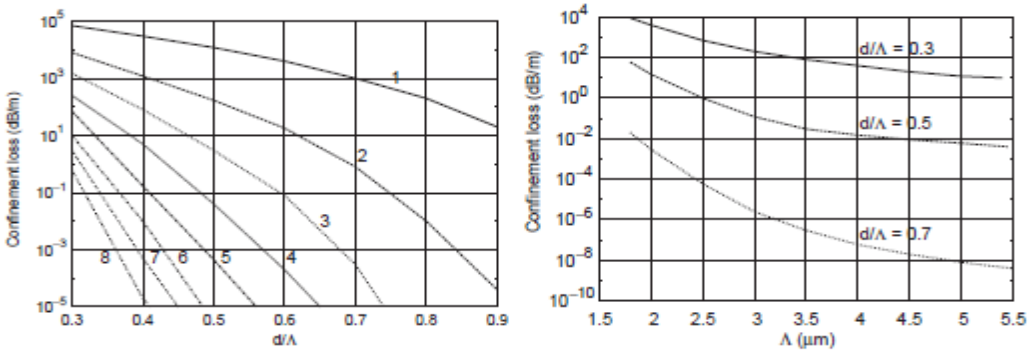

(i) (ii)

Figure 3(p): Leakage loss at 1550 nm (i) as a function of the air-hole diameter d normalized to the pitch Λ = 2.3 μm for different ring numbers and (ii) as a function of the pitch Λ for different air-filling fraction d/Λ [32].

As shown in Fig. 3(p{i}), its leakage loss quickly decreases when the air-hole ring number or the air-hole diameter increases. The reduction rate of the confinement loss increases in the same way with these geometric parameters. As expected, the loss decreases with larger Λ values for a fixed d/Λ. In this case, Λ and d are scaled in the same way, so a larger pitch corresponds to a larger silica core size and, as a consequence, to a higher field confinement. When the defect state moves closer to the PBG edges, the loss increases more quickly when the air-hole ring number is higher.

Despite the high air-filling fraction, that is d/Λ = 0.9, the dependence on the ring number is very weak, if compared with the case of solid-core PCFs. Finally, it is important to underline that there is a strong wavelength dependence of the loss. For example, the loss of the seven

air-hole ring PCF increases of a decade with respect to the minimum value in a wavelength range of less than 100 nm [32].

Bending Loss

As already stated, an alternative route to fabricate LMA fibers is offered by PCFs, which can be designed to be endlessly single-mode, unlike conventional fibers that exhibit a cutoff wavelength below which higher-order modes are supported. As for standard optical fibers, the practical achievable mode area in PCFs is limited by the macro bending loss [33].

Conventional fibers suffer additional loss if bent more tightly than a certain critical radius. The same behavior is observed also in PCFs, which show even a short-wavelength bend loss edge [33], caused by bend-induced coupling from the fundamental to the higher-order modes which leak out of the core. In fact, at short wavelengths the guided mode is mainly confined into the silica [33] and when $\lambda << \Lambda$ the field can escape through the interstitial space between the neighboring air-holes. As a consequence, the fiber becomes more sensitive to bending. Since LMA PCFs are generally designed with $\Lambda > 7 - 8$ μm, the standard telecommunication window falls in the short-wavelength edge. In spite of that, it has been demonstrated that LMA PCFs exhibit bending losses comparable with those of similarly sized conventional fibers at 1550nm [33].

PCFs with larger relative air-hole diameters that is with higher d/Λ, are less sensitive to bending loss. However, the demand for single-mode operation and the need for large-mode size limit the increase of d/Λ, and other solutions must be adopted. It has been demonstrated that the bending losses of triangular PCFs can be improved by changing the air-hole configuration from the traditional single-rod core design [34]. An accurate evaluation of the advantages regarding the bending loss can be obtained by comparing suitably matched three-rod and single-rod PCFs designs [34]. Many different approaches have been proposed in literature to evaluate the bending loss in conventional optical fibers, which usually assume a circular symmetric refractive index profile. Unfortunately, these approaches are not straightforward in PCFs, due to the complex nature of their refractive index profile. As a consequence, an accurate modeling of bending loss becomes even more challenging.

The transition loss occurs where the curvature of the fiber changes suddenly, that is at the beginning or the end of the bend. This loss can be modeled as a sort of coupling loss, because the mode fields in the straight and curved sections are not aligned. The pure bend loss is the continuous loss that occurs along any curved section of fiber due to the inability of the tails of the field to keep in phase with the faster-travelling central portion of the field. In this model, the full refractive index profile of the PCF is retained and hence the six fold field shape as well. In fact, the bent fiber is modeled as a straight fiber with an equivalent index profile given by a transformation that superimposes a gradient onto the refractive index of the straight fiber in the direction of the bend. Other theoretical approaches have been developed, which provide a correct parametric dependence of the bending loss with the PCF geometric parameters [34].

Hollow-core PCFs have different bending properties with respect to silica core ones. For applications like high-power delivery for medical use or material processing, which are suitable for air-guiding fibers, a low bending sensitivity is required, since it allows a very flexible use and an easy integration in supporting mechanical systems. After an early demonstration in a theoretical work of the low influence of bending on the hollow-core PCF guiding properties, the bending loss of air-guiding fibers have been experimentally measured [34]. The most important effect obtained with bending is a shift of the short-wavelength bandgap edge towards longer wavelengths, thus causing a PBG narrowing for the hollow-core PCFs. On the contrary, a similar shift has not been measured at the long-wavelength bandgap edge. In order to understand the fact that air-guiding PCFs are bending insensitive over most of the PBG, it is useful to consider the difference between the refractive index of the core and of the PBG edge, which corresponds to the cladding. Being this difference very high which is about 2×10^{-2}, a very tight confinement of the guided-mode in the hollow-core can be obtained, which results in the robust guiding even through tightly bent PCFs [34].

3.9 Material Models

One of the main advantages of the FDTD approach is the lack of approximations for the propagating field—light is modeled in its full richness and complexity. The other significant advantage is the great variety of materials that can be consistently modeled within the FDTD

context. In this sub-section we make a brief review of some of the main material properties that can be handled.

LOSSY DIELECTRICS:-

Before proceeding with a more detailed description it should be emphasized that the fact that in the time domain all the fields (H_x, E_y, H_z) are real quantities. Thus, accounting for loss is possible only through a non-zero conductivity σ of the medium:

$$\nabla \times H = \varepsilon_0 \varepsilon_r \frac{\partial E}{\partial t} + \sigma E = i\omega\varepsilon_0\left(\varepsilon_r - i\omega\varepsilon_0\varepsilon_{eff}E\right) \qquad (2)$$

Where

$$\varepsilon_{eff} = \varepsilon_r - i\frac{\sigma}{\omega\varepsilon_0} = \varepsilon_e^{Re} + i\varepsilon_r^{Im} = (n + ik)^2$$

We have assumed that

$$E \propto e^{iwt}$$

and

$$\frac{\partial}{\partial x} \rightarrow i\omega$$

corresponds to time-to-frequency domain Fourier transform. The real and imaginary part of the permittivity can be expressed through the real and imaginary part of the refractive index:

$$\varepsilon_r^{Re} = n^2 - k^2, \varepsilon_r^{Im} = 2nk, k = -\sigma/2\varepsilon_0\omega n \qquad (3)$$

This makes the refractive index approach and the conductivity approach equivalent.

LORENTS DISPERSION MATERIALS:-

By Lorentz dispersion materials, we mean materials for which the frequency dependence of the dielectric permitivity can be described by a sum of multiple resonance Lorentzian functions:

$$\varepsilon_r(\omega) = \varepsilon_\infty + \sum_{m=1}^{N} \frac{\chi_0 G_m \omega_{0m}^2}{\omega_{0m}^2 + i\Gamma_m\omega - \omega^2}, \sum_{m=1}^{N} G_m = 1 \qquad (4)$$

Where

ω_{0m} the resonant frequencies

G_m related to oscillators strengths

Γ_m Damping Coefficient

ε_∞ is the permittivity at infinite frequency.

$\chi_0 = \varepsilon_s - \varepsilon_\infty$ is permittivity at $\omega = 0$

In the lossless case Equation 8 is directly related to the Sellmeier equation which in the three resonances can be presented as:

$$n^2 = \varepsilon_\infty + \frac{A_1\lambda^2}{\lambda^2 - \lambda_1^2} + \frac{A_2\lambda^2}{\lambda^2 - \lambda_2^2} + \frac{A_2\lambda^2}{\lambda^2 - \lambda_3^2}\ , A_m = \chi_0 G_m (m = 1,2,3) \qquad (5)$$

In the lossy case, the Sellmeier equation can be written in a generalized form, accounting for a non-zero damping coefficient Γ_m as well as for anisotropy in the dispersion properties:

$$n^2(\omega) = \varepsilon_\infty + \frac{A_1\lambda^2}{\lambda^2 + i\Gamma_{\lambda 1}\lambda - \lambda_1^2} + \frac{A_2\lambda^2}{\lambda^2 + i\Gamma_{\lambda 2}\lambda - \lambda_2^2} + \frac{A_2\lambda^2}{\lambda^2 + i\Gamma_{\lambda 3}\lambda - \lambda_3^2} \qquad (6)$$

There are different ways to implement Equation 8 into the FDTD formalism. Here we consider the so-called polarization equation approach in the single resonance case. It uses the dielectric susceptibility function:

$$\chi(\omega) = \frac{\chi_0\omega_0^2}{\omega_0^2 + i\Gamma_m\omega - \omega^2} \qquad (7)$$

and the relation between the polarization and the electric field $P_y = \varepsilon_0\chi(\omega)E_y$. Taking the Fourier transform of the last equation leads to the following differential equation:

$$\frac{\partial^2 P_y}{\partial t^2} + \Gamma\frac{\partial P_y}{\partial t} + \omega_0^2 P_y = \varepsilon_0\chi_0\omega_0^2 E_y \qquad (8)$$

Where $\frac{\partial P_y}{\partial x} = J_y$

$$\frac{\partial J_y}{\partial x} + \Gamma J_y + \omega_0^2 P_y = \varepsilon_0\chi_0\omega_0^2 E_y \qquad (9)$$

Then Equation 9 is solved numerically together with the modified Equation 2:

$$\frac{\partial H_x}{\partial z} - \frac{\partial H_z}{\partial x} = \frac{\partial D_y}{\partial t} = \frac{\partial E_y}{\partial t} + \frac{\partial P_y}{\partial t} \qquad (10)$$

The FDTD approach can also account for a large variety of materials such as Drude dispersion materials, perfect metal, second-order, and third-order materials.

Nonlinear material model

In general, the nonlinear behavior is due to the dependence of the polarization P(t) on the applied electric field, E(t). Assuming an isotropic dispersive material, Maxwell's equations are:

$$\mu_0 \frac{\partial \vec{H}}{\partial t} = -\nabla \times \vec{E} \qquad (11)$$

$$\frac{\partial \vec{D}}{\partial t} = \nabla \times \vec{H} \qquad (12)$$

$$\vec{D} = \vec{P}^L + \vec{P}^{NL} + \sum_{m=1}^{M} \vec{P}_m^D \qquad (13)$$

$$\frac{\partial^2 \vec{P}_m^L}{\partial t^2} + \Gamma_m \frac{\partial \vec{P}_m^L}{\partial t} + \omega_m^2 \vec{P}_m^L = \varepsilon_0 \chi_0 G_m \omega_m^2 \vec{E} \qquad (14)$$

where represents the linear polarization, in general $\vec{P}^L = \varepsilon_0 \varepsilon_L \vec{E}$, $\vec{P}_m^D$ is the dispersive polarization which is controlled by Lorentz model in Equation 14 and denotes the nonlinear polarization.

The nonlinear polarization $\vec{P}_m^{NL}$ may come from various model sources that produce the different nonlinear phenomenon. These are:

- Dispersive second-order nonlinear material
- Dispersive third-order nonlinear material
- Dispersive Kerr effect
- Dispersive Raman Effect

Dispersive second-order nonlinear material

In this model, the electrical displacement D is

$$\vec{D} = \varepsilon_0 \varepsilon_L \vec{E} + \varepsilon_0 \chi^{(2)} : \vec{E}\vec{E} + \sum_{m=1}^{M} \vec{P}_m^D \qquad (15)$$

Where, ε_L is the linear relative permittivity and $\chi^{(2)}$ is the second order isotropic susceptibility. They are the real values. In order to simulate second order nonlinear effect, you should input two parameters: the linear relative permittivityε_L and the second order isotropic susceptibility $\chi^{(2)}$.

Dispersive third-order nonlinear material

Like the second-order nonlinearity, OptiFDTD takes third-order susceptibility to calculate the nonlinear polarization

$$\vec{D} = \varepsilon_0 \varepsilon_L \vec{E} + \varepsilon_0 \chi^{(3)} : \vec{E}\vec{E}\vec{E} + \sum_{m=1}^{M} \vec{P}_m^D \qquad (16)$$

Where, ε_L is the linear relative permittivity and $\chi^{(3)}$ is the third order isotropic susceptibility.

Dispersive Kerr effect

If the time scale over which the medium changed is greater than the pulse width, we should take into account the effects of the finite response time of the medium. Followed by Prof. Richard W. Ziolkowski 's work [35][36], OptiFDTD treats the nonlinear effect with a finite response time as well as an instantaneous manner by solving the phenomenological susceptibility equation simultaneously with Maxwell's equation:

$$\vec{D} = \varepsilon_0 \varepsilon_L + \vec{P}^{NL} + \sum_{m=1}^{M} \vec{P}_m^D \qquad (17)$$

$$\vec{P}^{NL} = \varepsilon_0 \chi^{NL} (\vec{\boldsymbol{r}}, \boldsymbol{t}, |\boldsymbol{E}|^{\mathbf{2}}) \vec{E} \qquad (18)$$

$$\frac{\partial \chi^{NL}}{\partial t} + \frac{1}{\tau} \chi^{NL} = \frac{1}{\tau} \varepsilon_2 |E|^2 \qquad (19)$$

Where,

ε_L is the linear relative permittivity

χ^{NL} is the nonlinear susceptibility

τ is the response time

ε_2 is the Kerr model permittivity.

Dispersive Raman Effect

Raman model allows another way to simulate the nonlinear phenomenon where the nonlinear susceptibility was modeled by a second-order derivative equation which is related to the resonant wavelength and the response time

$$\vec{D} = \varepsilon_0 \varepsilon_L + \vec{P}^{NL} + \sum_{m=1}^{M} \vec{P}_m^D \qquad (20)$$

$$\vec{P}^{NL} = \varepsilon_0 \chi^{NL} \vec{E} \qquad (21)$$

$$\frac{\partial^2 \chi^{NL}}{\partial t^2} + \tau_R \omega_R^2 \frac{\partial \chi^{NL}}{\partial t} + \omega_R^2 \chi^{NL} = \boldsymbol{\varepsilon}_R \omega_R^2 |E|^2 \qquad (22)$$

Where,

ε_L is the linear relative permittivity

χ^{NL} is the nonlinear susceptibility

τ is the response time

ε_R is the Raman model permittivity

ω_R is the Raman model resonant frequency.

LORENTZ DRUDE MODEL:-

L-D Model in frequency domain

It has been shown [37] that a complex dielectric functions for some metals and surface plasmas can be expressed in the following form:

$$\varepsilon_r(\omega) = \varepsilon_r^f(\omega) + \varepsilon_r^b(\omega) \qquad (23)$$

This form separates explicitly the intraband effects (usually referred to as free electron effects) from interband effect (usually referred to as bound-electron effects). The intraband part $\varepsilon_r^f(\omega)$ of the dielectric function is described by the well know free-electron or Drude model [38] [39]:

$$\varepsilon_r^f(\omega) = 1 + \frac{\Omega_p^2}{j\omega\Gamma_0 - \omega^2} \qquad (24)$$

The interband part of the dielectric function is described by the simple semiquantun model resembling the Lorentz results for insulators:

$$\varepsilon_r^f(\omega) = \left(\sum_{m=1}^{M} \frac{\Omega_p^2}{\omega_m^2 - \omega^2 + j\omega\Gamma_m}\right) \qquad (25)$$

Where, $\omega_p$is plasma frequency, m is the number of oscillators with frequency ω_m and lifetime $1/\Gamma_m$, where $\Omega_p = \sqrt{G_m}\omega_p$ is the plasma frequency as associated with intraband transitions with oscillator strength G_0 and damping constant Γ_0

The above L-D model can be expressed as more general equation as:

$$\varepsilon_r(\omega) = \varepsilon_{r,\infty} + \sum_{m=0}^{M} \frac{G_m\Omega_m^2}{\omega_m^2 - \omega^2 + j\omega\Gamma_m} \qquad (26)$$

Here $\varepsilon_{r,\infty}$ is the relative permittivity in the infinity frequency, Ω_m is the plasma frequency, ω_m is the resonant frequency, and Γ_m is the damping factor or collision frequency.

In this general equation, if only the term $m = 0$ exists, and $\omega_0 = 0$, then the general equation describes the Drude model as in (24). If only the $m = 1 \ldots M$ term exists, and $\Omega_1 = \Omega_2 = \cdots = \Omega_M$; then the general model becomes the Lorentz model as in (25). This model can also work as the separate Drude and Lorentz models.

L-D Model in time domain

The Lorentz-Drude model in (26) is in the frequency domain. However, FDTD is a time domain method and therefore would be suitable for broadband simulations. We need to transform (26) to time domain so that FDTD can handle the fullwave-analysis for the Lorentz-Drude material. This transformation to time domain is accomplished by using the

Polarization philosophy within Maxwell's equation. The Lorentz-Drude model in time domain can be expressed:

$$\mu_0 \frac{\partial H}{\partial t} = \nabla \times E \qquad (27)$$

$$\varepsilon_{r,\infty}\varepsilon_0 \frac{\partial E}{\partial t} + \sum_{m=0}^{M} \frac{\partial P_m}{\partial t} = -\nabla \times H \qquad (28)$$

$$\frac{\partial^2 P_m}{\partial t^2} + \Gamma \frac{\partial P_m}{\partial t} + \omega_m^2 P_m = \varepsilon_0 G_m \Omega_m^2 E \qquad (29)$$

The FDTD algorithm can be derived based on the above equation.

PBG materials Applications

A growing array of imaging systems allows for the emergence of a set of less-invasive diagnostic procedures. Lasers are increasingly used in surgery that is more precise and less destructive than the scalpel. Unlike magnetic resonance imaging, which relies on very long wavelength radiations, or X-ray based tomography which depends on very short wavelength radiations, the optical matter utilizes intermediate wavelength windows. This window is sensitive to the concentration of oxygenated hemoglobin in the tissue and thereby provides an early diagnostic image of the metabolic process leading to cancer prior to structural damage caused by a tumor. Since these medical applications may yield health benefits, the need to promote the technology becomes more desirable. Some common applications include:

a. Zero-threshold microlasers with high modulation speed.
b. Low-threshold optical switches and all optical transistors for optical telecommunication.
c. High-speed optical computers.
d. Micro-lasers operating near a photonic band edge will exhibit ultra-fast modulation and switching speeds for application in high-speed data transfer and computing.
e. Applications such as telecommunications, transfer and computing will be greatly enhanced through all optical processing in which bits of information, encoded in the

form of a photon number distribution, can be transmitted and processed without conversion to and from electrical signals.

f. The PBG material provides dopant atom with a high degree of protection from damping effects of spontaneous emission and dipole de-phasing. In this case the two-level atoms may act as a two-level quantum mechanical register or single photon logic gate for all optical quantum computing.

g. Multiple scattering of light in biological tissue provides a safe, inexpensive and non-insidious probe of brain, breast and skin tumors.

CHAPTER

4

SIMULATION RESULTS AND COMPARISON

In this chapter, the two dimensional photonic Band gap Crystal Structure has been designed and modeled. The structure is designed as a finite difference time domain model using the LAYOUT DESIGNER of OptiFDTD tool. The PROFILE DESIGNER of OptiFDTD tool has been used to define channel as well as material, with user defined refractive index, that is used to design the structure. OptiFDTD Analyzer is used to study the transmittance and reflectance properties of the design and PWE Band Solver is used to study the band gap characteristics of the design. The anisotropic perfectly matched layers (APML) have been used as boundary conditions in all the designs.

4.1 Photonic Band Gap Structure Design

Photonic Band Gap (PBG) materials, also known as photonic crystals, are materials which have a band gap due to a periodicity in the materials dielectric properties. The band gap in photonic crystals represents the forbidden energy range where wave behaving photons cannot be transmitted through the material. This behaviour is equivalent to electrons in crystalline semiconductors and in the same manner PBG materials can be used to affect and control the movement of electromagnetic waves. By imitating the periodicity of photonic crystals one can tailor the specific band gap of a structure. This is done in PBG structures by defining a pattern with repeating regions which alternates between materials with high and low dielectric constant.
By defining the periodicity of the pattern one can therefore limit which specific photon frequencies are allowed to pass and which are not. The size of the band gap is determined by the difference in dielectric constant between the materials used. PBG structures in the optical regime have many applications and can be used in multi processing computing devices such as: low-loss waveguides, optical switches, filters and beam shaping for LEDs.

The waveguide channel is defined to be the material of different refractive index (n) or permittivity ($\varepsilon_r = n^2$) and the default wafer material is air with refractive index or permittivity 1.

Hence alternating layers of materials having permittivity contrast $1/n^2$ forms the layout of crystal. This crystal structure is known as Y branch Photonic Band Gap crystal. The wafer dimensions are 21µm × 15µm.

The layout is drawn taking the default Hexagonal lattice and specify the Lattice dimensions (17, 19). The input wave is taken to be Gaussian modulated continuous wave with wavelength 1900 nm. The layout is shown below.

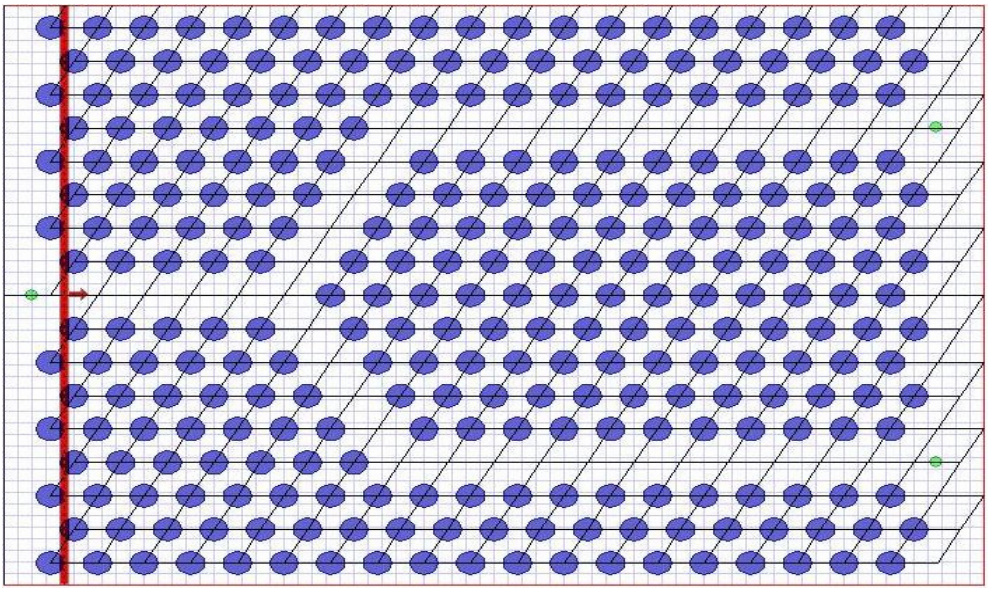

Figure 4(a): Layout of Y branch Photonic Band Gap crystal.

The computational domain in both 2D and 3D simulations is limited and has associated boundaries. Each of the boundaries can be set up independently to satisfy different boundary conditions. The boundary conditions in the simulation environment are set for the anisotropic perfectly matched layers (APML). The four parameters for the boundary conditions are set as:

- Number of PML Layers = 10
- Theoretical Reflection Coefficient = 1e-012
- Real APML Tensor Parameter = 5
- Power of the Grading Polynomial = 3.5

The OptiFDTD Simulator uses the APML to surround the FDTD lattice. The outer boundary of the APML is assumed to be a Perfect Conductor (PEC) wall that may cause some power to reflect back into the primary computation zone.

To observe the transmittance and reflectance properties of the defined structure, the FDTD simulation is done taking the TE waves. The mesh delta size is 0.1µm × 0.1µm and numbers of mesh cells are 150 × 210. The minimum memory requirements are 37.68MB and after size is 21µm × 15µm as already defined. The simulation is done for 10000 time steps.

4.2 For Germanium Crystals (Ge n=4.1):

In the layout the vertical dotted line having arrow at its centre is the input plane and the other vertical lines are unit cells of PBG lattice having refractive index 4.1 or permittivity 16.81 and the base material of lattice as shown by crossed area in between the shaded lines is the default material air with permittivity 1. Hence the permittivity contrast of 1/16.81 is formed in the design.

The refractive index distribution profile for the structure is shown in figure 4(b).

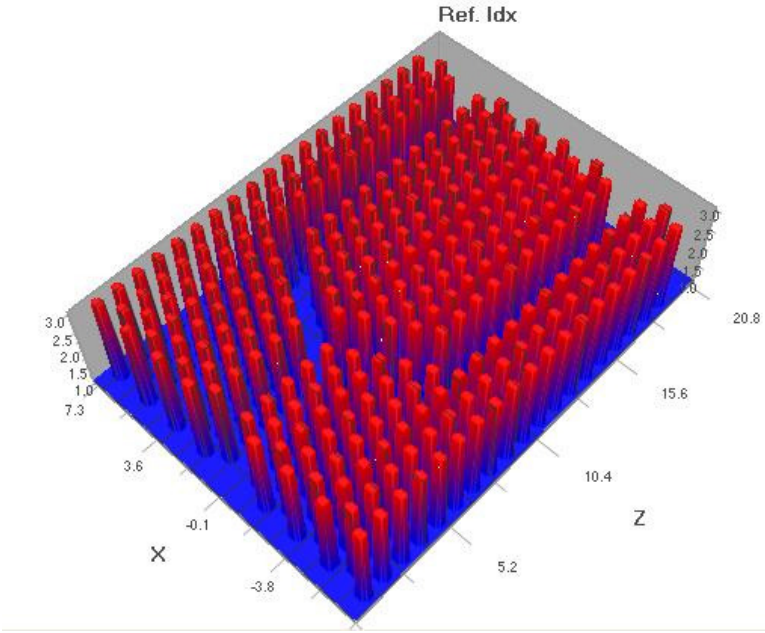

Figure 4(b): Refractive index distribution profile of designed Y branch PBG Crystal (Ge n=4.1).

The amplitude variation of Discretized Fourier Transform (DFT) output of all the components of TE wave and the poynting vector with the variations in Z-direction (position) at the end of simulation has been shown below.

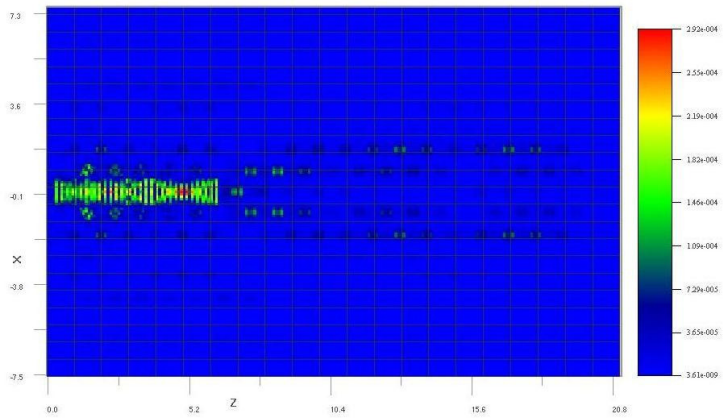

Figure 4(c): DFT output of Amplitude variation of H_x along horizontal plane.

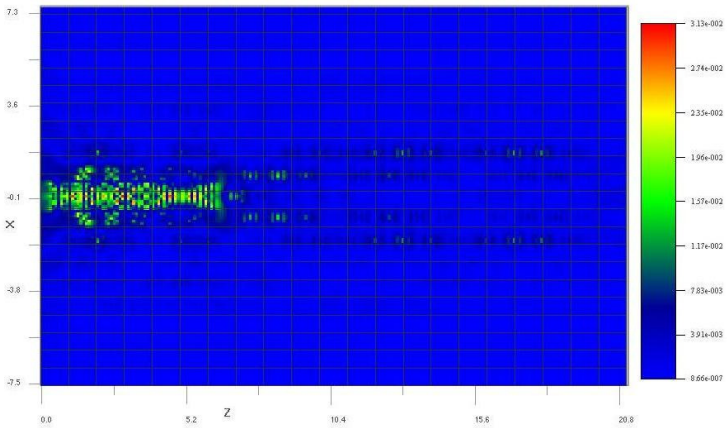

Figure 4(d): DFT output of Amplitude variation of E_y along horizontal plane.

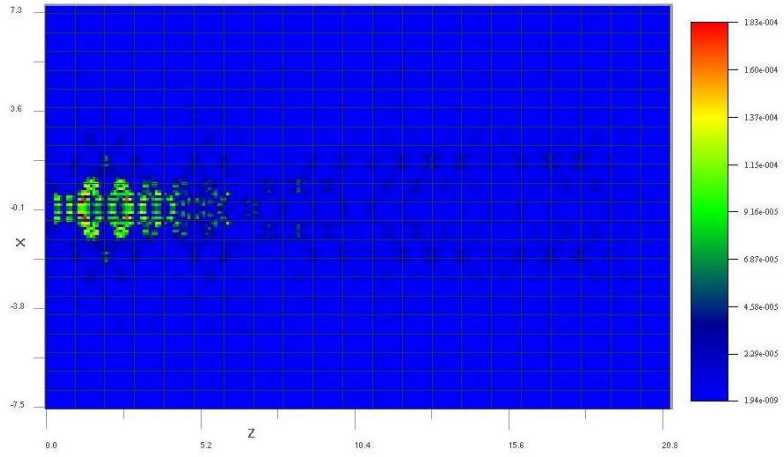

Figure 4(e): DFT output of Amplitude variation of H_z along horizontal plane.

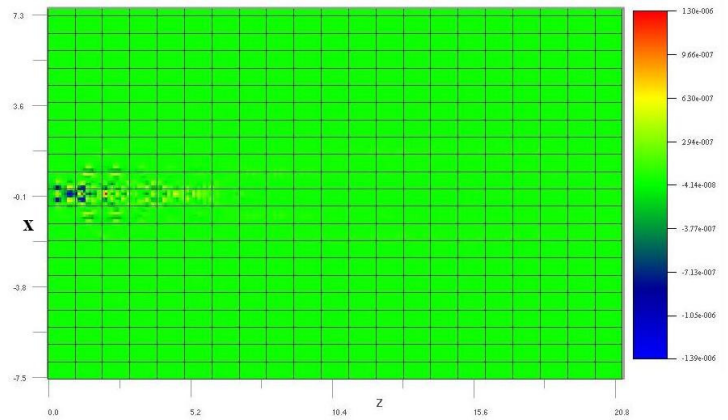

Figure 4(f): Variation of Poynting Vector along horizontal plane.

These outputs indicate how the wave components will be varied for the designed photonic structure that is how the electric and magnetic field components are varied with horizontal plane. It has been observed that the DFT amplitude is higher at beginning and fall as soon as the wave falls on the first horizontal layer and after that minor variations are there as the wave passes through the alternating layers of air and defined material.

Figure 4(f) shows the variations of poynting vector that is just higher at the beginning and dies very soon.

Next the band gap characteristics of defined photonic band gap structure are observed and are done by Plane Wave Expansion (PWE) method. The PWE band solver simulation is done for the same and band gaps are observed. The PWE band solver has taken PBG structure and TE polarization. The mesh delta size is taken to be 0.0625µm in vertical direction and numbers of mesh steps are taken as 16. For the tolerance value 0.1 the band solver output is as follows

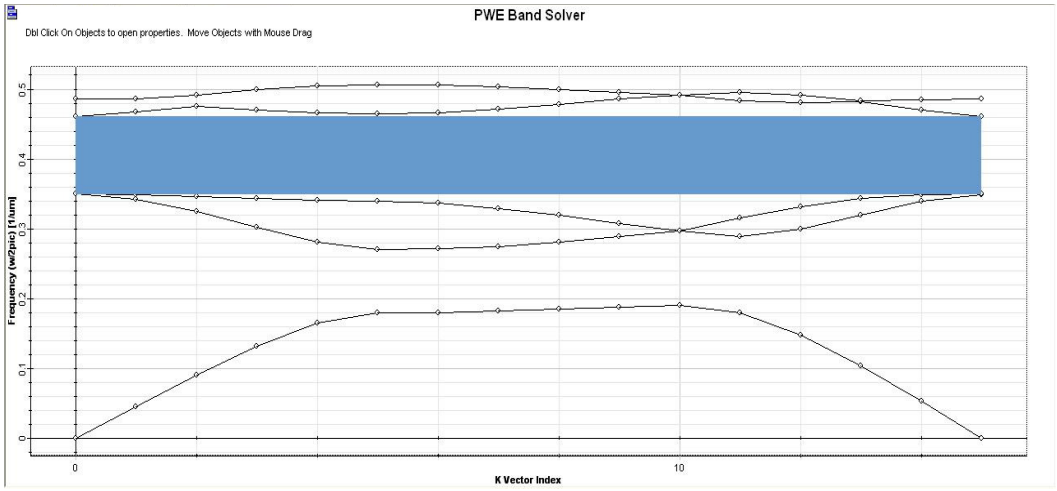

Figure 4(g): Band diagram of photonic band gap crystal (Ge n=4.1).

Only one band gap is found as shown by shaded area in the graph. The number of band gaps found could depend on tolerance value. The band gap result summary is shown below

```
□□Band gap 0: (0.190239, 0.27017), gap = 0.0799312:        Thursday, June 09, 2011 at 21:27:44
□□Band gap 1: (0.350505, 0.461244), gap = 0.110739:        Thursday, June 09, 2011 at 21:27:44
Tolerance = 0.1: Band gap(s) found = 1:          Thursday, June 09, 2011 at 21:27:51
□□Band gap 0: (0.350505, 0.461244), gap = 0.110739:        Thursday, June 09, 2011 at 21:27:51
```

Figure 4(h): Band Gap result summary of photonic band gap crystal (Ge n=4.1).

So the band gap defines the frequency range for the design corresponding to which the wave gets strongly reflected. For the frequency range or band gap as shown in figure 4(h), the input wave having frequency outside this range will get strongly reflected.

4.3 For Gallium Arsenide Crystals (GaAs n=3.3):

In the layout the vertical dotted line having arrow at its centre is the input plane and the other vertical lines are unit cells of PBG lattice having refractive index 3.3 or permittivity 10.89 and the base material of lattice as shown by crossed area in between the shaded lines is the default material air with permittivity 1. Hence the permittivity contrast of 1/10.89 is formed in the design.

The amplitude variation of Discretized Fourier Transform (DFT) output of all the components of TE wave and the poynting vector with the variations in Z-direction (position) at the end of simulation has been shown below.

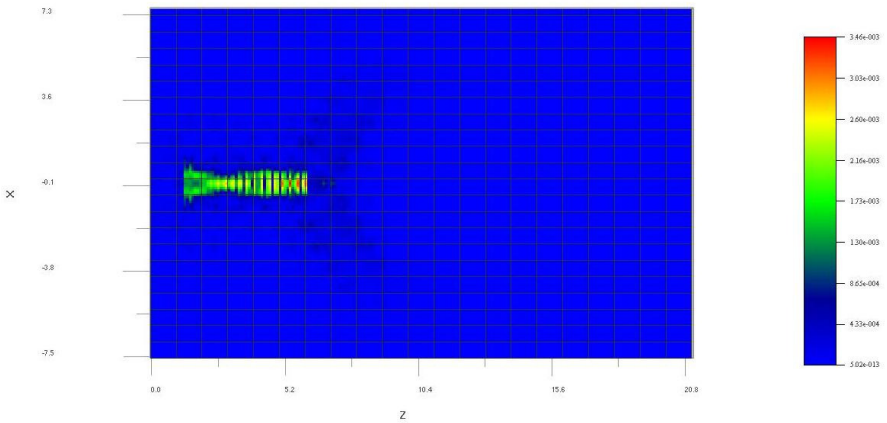

Figure 4(i): DFT output of Amplitude variation of H_x along horizontal plane (GaAs n=3.3).

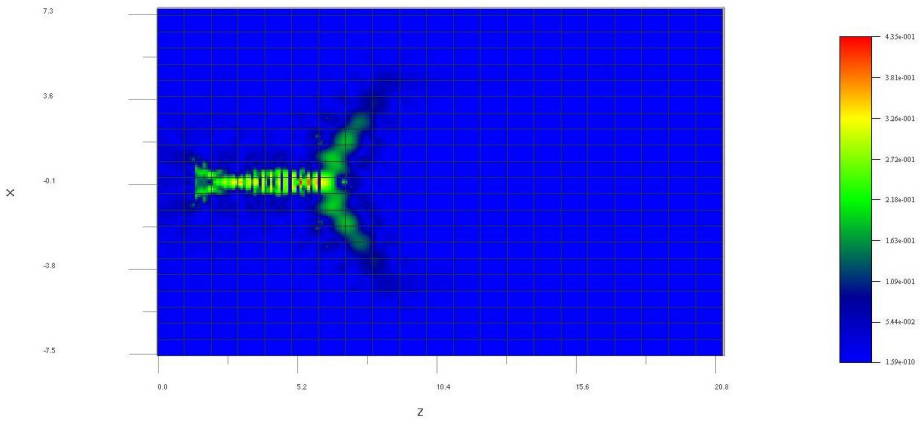

Figure 4(j): DFT output of Amplitude variation of E_y along horizontal plane (GaAs n=3.3).

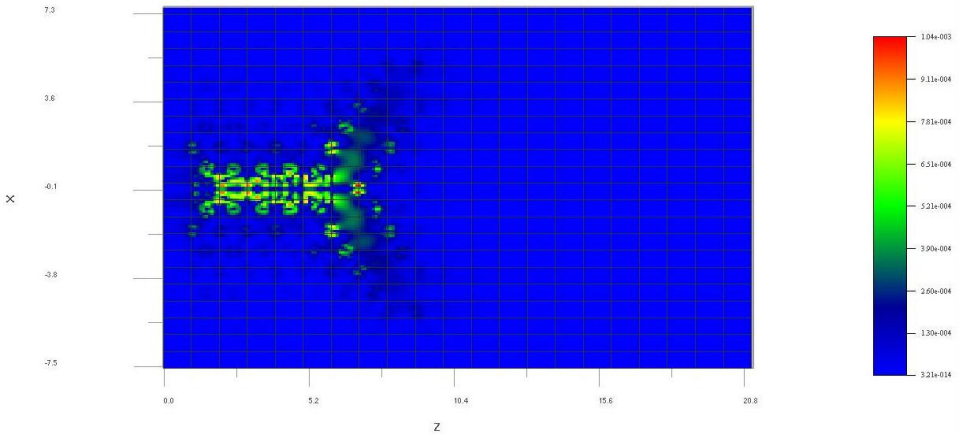

Figure 4(k): DFT output of Amplitude variation of H_z along horizontal plane (GaAs n=3.3).

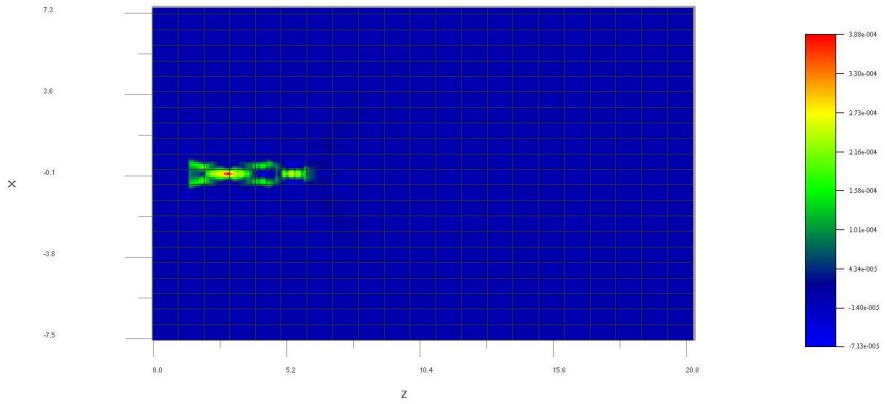

Figure 4(l): Variation of Poynting Vector along horizontal plane (GaAs n=3.3).

These outputs indicate how the wave components will be varied for the designed photonic structure, that is how the electric and magnetic field components are varied with horizontal

plane. It has been observed that the results are better than that of results obtained with constant refractive index (n= 4.1) of Germanium.

Figure 4(l) shows the variations of poynting vector that is just maximum at the beginning and dies gradually even before it reaches the node.

Next the band gap characteristics of defined photonic band gap structure are observed and are done by Plane Wave Expansion (PWE) method. The PWE band solver simulation is done for the same and band gaps are observed. The PWE band solver has taken PBG structure and TE polarization. The mesh delta size is taken to be 0.0625µm in vertical direction and numbers of mesh steps are taken as 16. For the tolerance value 0.1 the band solver output is as follows

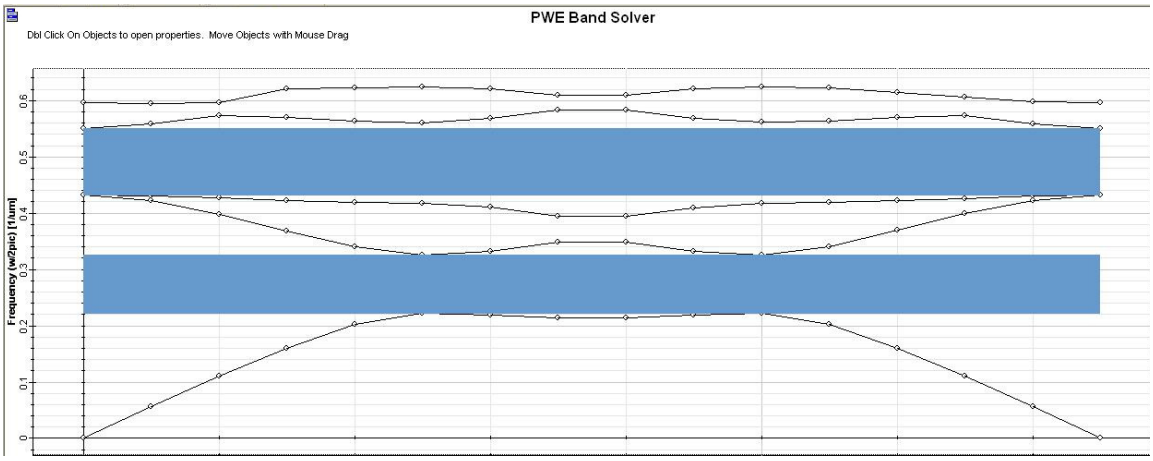

Figure 4(m): Band diagram of photonic band gap crystal (GaAs n=3.3).

Two band gaps are found as shown by shaded area in the graph. The number of band gaps found could depend on tolerance value. The band gap result summary is shown below

Figure 4(n): Band Gap result summary of photonic band gap crystal (GaAs n=3.3).

So the band gap defines the frequency range for the design corresponding to which the wave gets strongly reflected. For the frequency range or band gap as shown in figure 4(n), the input wave having frequency outside this range will get strongly reflected.

4.4 For Gallium Phosphide Crystals (GaP n=3.1):

The only difference in this PBG lattice is that every unit cell in the lattice is having refractive index 3.1 or permittivity 9.61 and the base material of lattice is the default material air with permittivity 1. Hence the permittivity contrast of 1/9.61 is formed in the design.

The amplitude variation of Discretized Fourier Transform (DFT) output of all the components of TE wave and the poynting vector with the variations in Z-direction (position) at the end of simulation has been shown below.

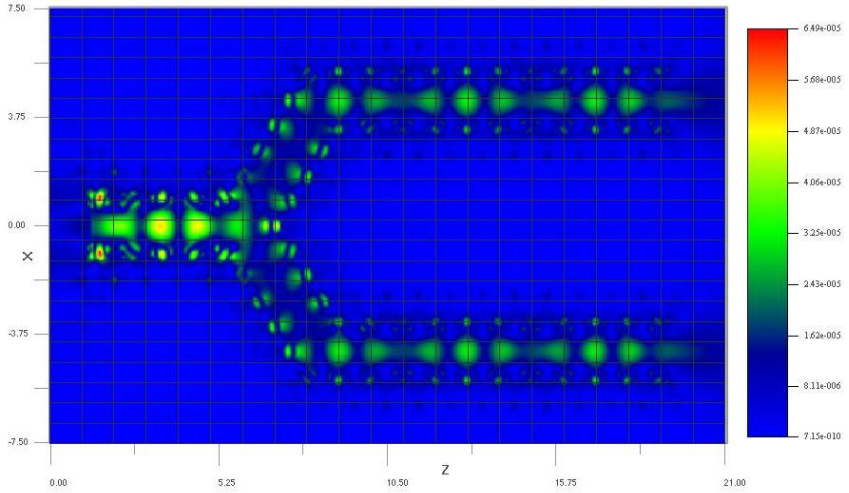

Figure 4(o): DFT output of Amplitude variation of H_x along horizontal plane.

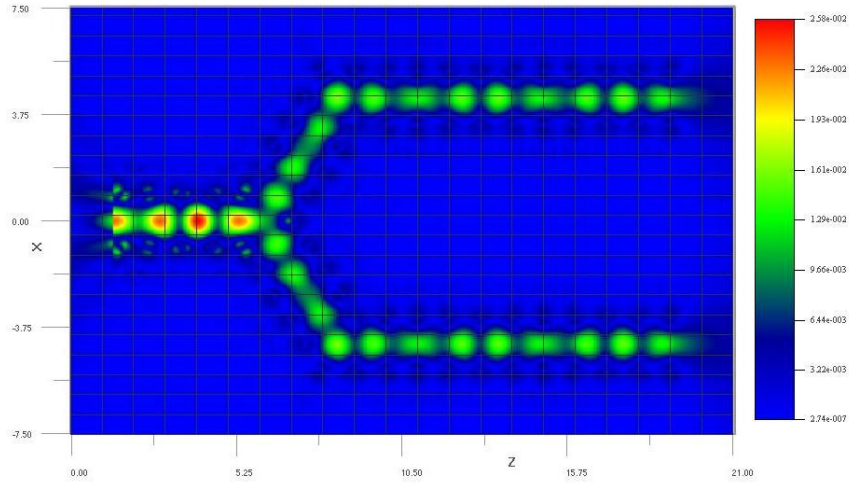

Figure 4(p): DFT output of Amplitude variation of E_y along horizontal plane.

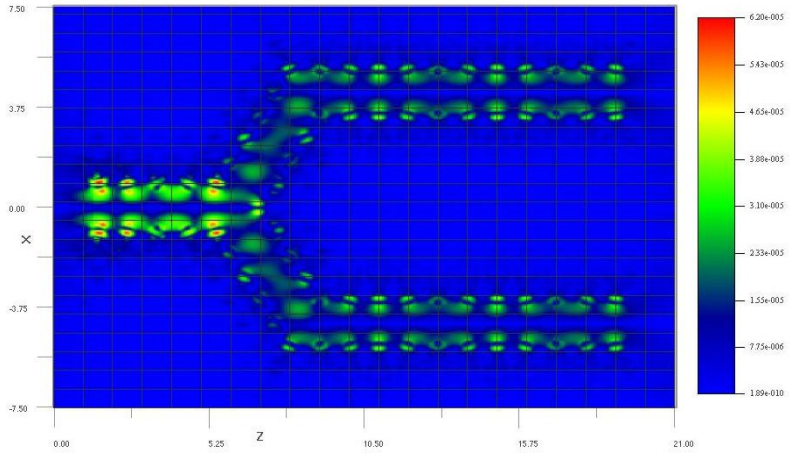

Figure 4(q): DFT output of Amplitude variation of H_z along horizontal plane.

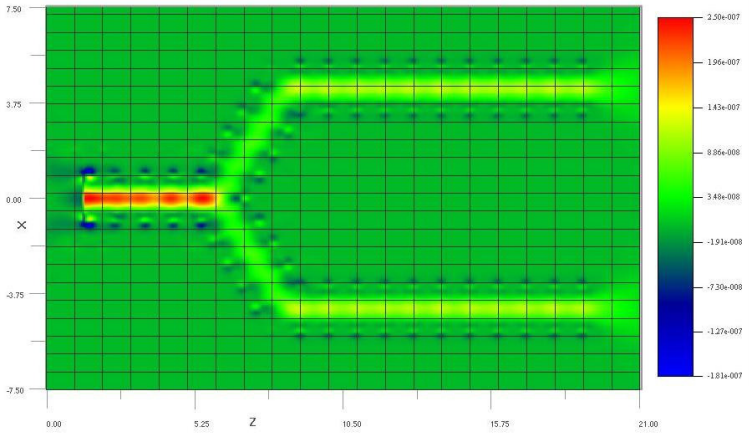

Figure 4(r): Variation of Poynting Vector along horizontal plane.

These outputs indicate how the wave components will be varied for the designed photonic structure, that is how the electric and magnetic field components are varied with horizontal plane. It has been observed that the results are better than that of results obtained with both Germanium and Gallium Arsenide. Figure 4(r) shows the variations of poynting vector that is equally distributed throughout the wave path designed that is the TE waves travel through the wave path with minimum dispersion and absorption.

Next the band gap characteristics of defined photonic band gap structure are observed and are done by Plane Wave Expansion (PWE) method. The PWE band solver simulation is done for the same and band gaps are observed. The PWE band solver has taken PBG structure and TE polarization. The mesh delta size is taken to be 0.0625µm in vertical direction and numbers of mesh steps are taken as 16. For the tolerance value 0.1 the band solver output is as follows

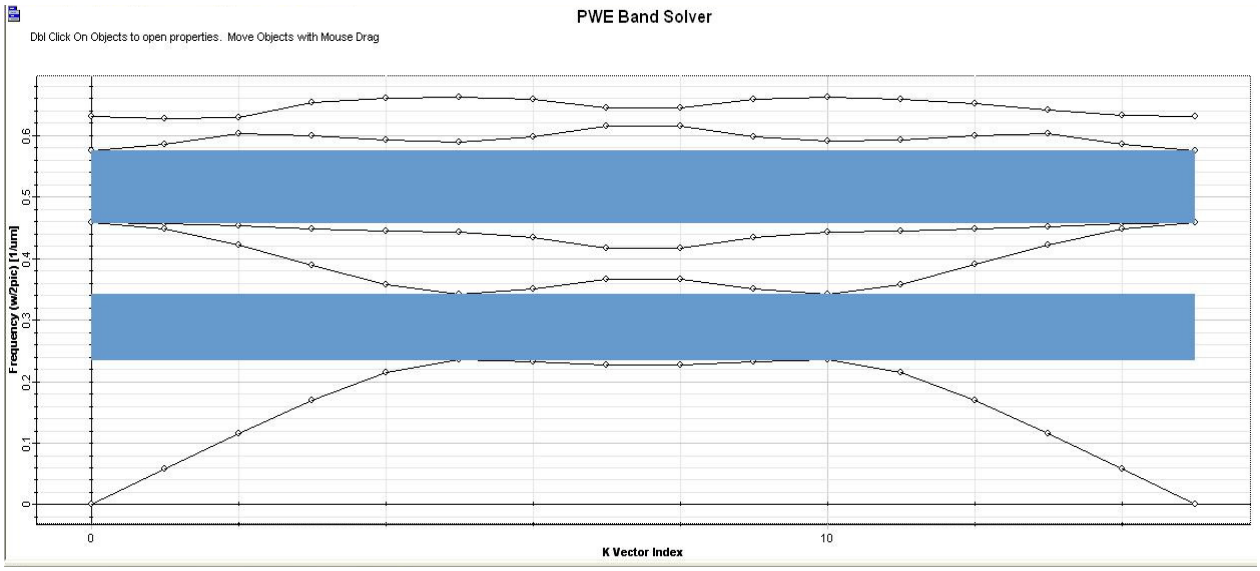

Figure 4(s): Band diagram of photonic band gap crystal (GaP n=3.1).

Two band gaps are found as shown by shaded area in the graph. The number of band gaps found could depend on tolerance value. The band gap result summary is shown below

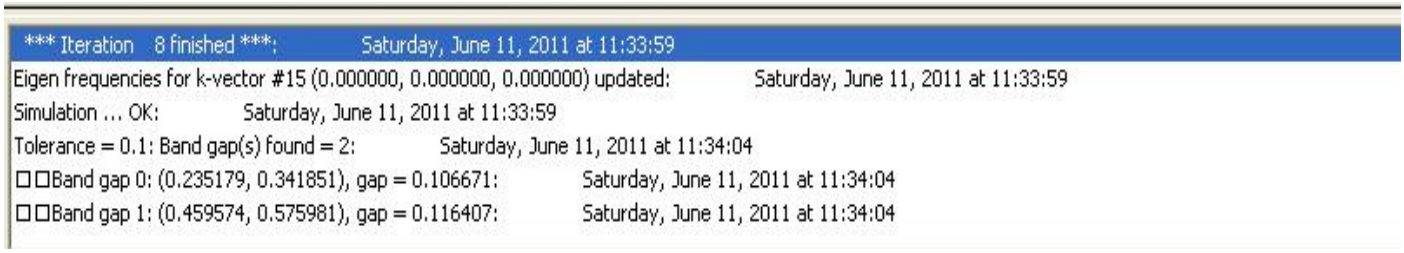

Figure 4(t): Band Gap result summary of photonic band gap crystal (GaP n=3.1).

So the band gap defines the frequency range for the design corresponding to which the wave gets strongly reflected. For the frequency range or band gap as shown in figure 4(t), the input wave having frequency outside this range will get strongly reflected.

4.5 The Band Gap Analysis- A Comparison

As the mode analysis and band gap analysis is done for three different materials with constant refractive index, the band gap characteristics have been improved from higher refractive index to lower refractive index. Since the band gap analysis is done for photonic applications in multiprocessor computing a wider and multiple band gaps are observed at the end. A comparison is shown in the table 4.1 for all three designs.

Table 4.1: Band Gap Comparison for Designed PBG crystals.

PBG Structure Material	Ref. Index	No. of Band Gaps	Bandgap Range	Gap	Tolerance
Germanium	4.1	1	0.350505, 0.461244	0.110739	0.1
Gallium Arsenide	3.3	2	0.221574, 0.325075 0.432768, 0.549614	0.1035 0.116847	0.1
Gallium Phosphide	3.1	2	0.235179, 0.341851 0.459574, 0.575981	0.106671 0.116407	0.1

As the table indicates, it can be easily concluded that no. of band gaps as well as band gap frequency range comes out to be maximum for the PBG crystal designed using GaP (Gallium Phosphide) which makes it a desirable choice for photonic multiprocessor application.

CHAPTER 5

CONCLUSION

Silicon has been the mainstay of the electronics industry for the last 40 years and has revolutionized the way the world operates. Today a silicon chip the size of a fingernail contains nearly one billion transistors and has the computing power that only a decade ago would take up an entire room full of servers. In addition the silicon integrated chip has moved beyond just computer microprocessors to impact everything from cell phones to music players to cameras. Silicon photonics is the emerging technology of producing optical devices and circuits using silicon as the core material with standard CMOS (complementary metal oxide semiconductor) manufacturing equipment and processes. Silicon photonics, based mainly on silicon on insulator (SOI), has recently attracted a great deal of attention. The intrinsic bandgap of silicon (1.1 eV) means that silicon is transparent at wavelengths typically used for optical communication transmission (i.e., 1270 nm to 1625 nm). This allows one to build optical devices in silicon that can route, direct and manipulate light. The utilization of standard CMOS compatible process for silicon photonics allows an incomparable monolithic integration of photonics devices with electronic control functions that offer an opportunity for low-cost optoelectronic solutions. Silicon's main drawback is its poor optical emission efficiency due to its indirect band-gap. Bands are separated not just by energy but also by momentum- photon emission requires the participation of phonons, hence, orders of magnitude lower radiative emission probability than with direct semiconductors.

Most multiprocessor communications operate in the near-infrared (NIR) wavelength (around 0.85, 1.31, and 1.55 μm), a region where silicon is a poor detector. In order to improve the performance of silicon-based detectors, the most common approach is to grow germanium (Ge) on the Si and to use the Ge narrower bandgap to extend the maximum detectable wavelength. Today various groups have already reported on Ge-on-Si (NIR) detectors, with responsivity nearly equivalent to those of III–V based devices.

CONCLUSION

From above comparisons of FDTD modeled photonic band gap wave guide with different refractive index. It is clear that (GaP) gallium phosphide shows better optical efficiency then its counterpart's i.e germanium and Gallium Arsenide for Far infrared (FIR) wavelength i.e 1900 nm in particular in the simulations done in this research work.

REFERENCES

[1] J. Knight, T. Birks, B. Mangan and P. St. James Russell, "New solutions in fiber optics," Optics Photonics News, vol. 13, pp. 26–30, Mar. 2002.

[2] Jeremiah K. Jones, "Photonic Computing" English 316, Process Explanation.

[3]Sudeep Pasricha, Nikil Dutt "ORB: An On-chip Optical Ring Bus Communication Architecture for Multi-Processor Systems-on-Chip", 2008

[4] Bahram Jalali, Sasan Fathpour, "Silicon Photonics", journal of lightwave technology, vol. 24, no. 12, december 2006

[5] Intel Corporation, White Paper "The 50G Silicon Photonics Link" 2010

[6] K. Yee, "Numerical solution of initial boundary value problems involving Maxwell's equations in isotropic media," IEEE Trans. Antennas Propag., vol. AP-14, no. 3, pp. 302–307, May 1966.

[7] A. Taflove, "Application of the finite difference time domain method to sinusoidal steady state electromagnetic-penetration problems," IEEE Trans. Electromagn. Compat., vol. EMC-22, no. 3, pp. 191–202, Aug. 1980.

[8] B.M.dillion and J.P.Webb, "A comparison of formulation for vector finite element analysis of photonic waveguides", IEEE transactions on microwave theory and techniques, Vol.42, pp.308-316, Feb.1994.

[9] D. M. Sullivan, "Electromagnetic Simulation using the FDTD Method," Piscataway, NY: IEEE Press, 2000.

[10] A. Taflove and M. E. Brodwin, "Numerical solution of steady-state electromagnetic scattering problems using the time-dependent Maxwell's equations," IEEE Transactions on Microwave Theory and Techniques, vol. 23, pp. 623–630, Aug.1975

[11] K. R. Umashankar and A. Taflove, "A novel method to analyze electromagnetic scattering of complex objects". IEEE Transactions on Electromagnetic Compatibility, vol. 24, pp. 397–405, 1982.

[12] Taflove, Alen "Computational Electrodynamics: The FDTD method" Artech house, Boston, 1995.

[13] Zhili Lin, Chunxi Zhang, Pan Ou, Yudong Jia and Lishuang Feng. "A Generally Optimized FDTD Model for Simulating Arbitrary Dispersion sub wavelength model Based

on the Maclaurin Series Expansion" Journal Of Lightwave Technology, vol. 28, no. 19, October 1, 2010.

[14] D. H. Choi and W. J. Hoefer , "The finite difference time-domain method and its application to eigenvalue problems," IEEE Transactions on Microwave Theory and Techniques, vol.34, pp. 1464–1470, 1986.

[15] J. Berenger, "A perfectly matched layer for the absorption of electromagnetic waves". Journal of Computational Physics, vol. 114, pp. 185–200, Aug. 1994.

[16] S. D. Gedney, "An anisotropic perfectly matched layer absorbing media for the truncation of FDTD lattices," IEEE Transactions on Antennas and Propagation, vol. 44, pp. 1630–1639, 1996.

[17] B. Engquist and A. Majda, "Absorbing boundary conditions for the numerical simulation of symmetric waves," Math Comp, vol. 31, pp. 629-651, July 1977.

[18] R. R. McLeod, "Finite difference time domain boundary conditions class notes," pp. 31–59, Sept. 2004.

[19] G.P. Agarwal, "Non linear fiber optics", fourth edition, Academic press-UK, 2007.

[20] James R. Nagel, "The One-Dimensional Finite difference Time Domain(FDTD) Algorithm Applied to the telegrapher equation" university of Utah

[21] A. Soriano, "Analysis of the finite difference time domain technique to solve the Schroginer equation for quantum devices," Journal of Applied Physics, Vol. 95, N12, June 2004.

[22] S.Guo, S.Albin, "Simple plane wave implementation for photonic crystal calculations," Optics Express 11, no.2, p.167-175, 2003.

[23] D. H. Choi and W. J. Hoefer , "The finite-difference time-domain method and its application to eigenvalue problems" IEEE Transactions on Microwave Theory and Techniques, vol. 34, pp. 1464–1470, Nov. 1986.

[24] Okamoto K., "Fundamentals of Optical Waveguides," Academic Press, San Diego 2000.

[25] J. D. Joannopoulos, R. D. Meade, and J. N. Winn, "Photonic Crystals: Molding the Flow of Light," Princeton University Press, Princeton, NJ, 1995.

[26] P. St. J. Russell, "Photonic crystal fibers," Opt. Science, vol. 299, pp. 358–362, Jan. 2003.

[27] J. C. Knight, J. Broeng, T. A. Birks, and P. St. J. Russell, “Photonic band gap guidance in optical fibers,” Opt Science, vol. 282, pp. 1476–1478, Nov. 1998.

[28] W. H. Reeves, J. C. Knight, P. St. J. Russell and P. J. Roberts, “Demonstration of ultra-flattened dispersion in photonic crystal fibers,” Optics Express, vol. 10, pp. 609–613, July 2002.

[29] R. E. Kristiansen, K. P. Hansen, J. Broeng, P. M. W. Skovgaard, M. D. Nielsen, A. Petersson, T. P. Hansen, B. Mangan, C. Jakobsen and H. R. Simonsen, “Microstructured fibers and their applications,” in OPTOEL 2005, Elche, Spain, July 13–15, 2005.

[30] K. Kurokawa, K. Tajima, K. Tsujikawa and K. Nakajima, “Reducing the losses in photonic crystal fibres,” in Proc. European Conference on Optical Communication-ECOC 2005, Glasgow, Scotland, Sept. 25–29, 2005.

[31] K. Tajima, J. Zhou, K. Nakajima, and K. Sato, “Ultra low loss and long length photonic crystal fiber,” in Proc. Optical Fiber Communications Conference-OFC 2003, Atlanta, Georgia, USA, Mar. 23–28, pp. PD1.1–PD1.3, 2003.

[32] L. Vincetti, D. Ferrarini, M. Zoboli, A. Cucinotta, F. Poli, and S. Selleri, “Leakage losses in photonic band gap fibers,” in Proc. European Conference on Optical Communication-ECOC 2003, Rimini, Italy, Sept. 21–25, 2003.

[33] K. Miyake, M. Hachiwaka, T. Kinoshita, S. Yamaguchi, H. Kubota, and S. Kawanishi, “Bend resistant photonic crystal fiber compatible with conventional single mode fiber,” in Proc. European Conference on Optical Communication-ECOC 2004, Stockholm, Sweden, Sept. 5–9,
2004.

[34] T. P. Hansen, J. Broeng, C. Jakobsen, G. Vienne, H. R. Simonsen, M. D. Nielsen, P. M. W. Skovgaard, J. R. Folkenberg and A. Bjarklev, “Air-guiding photonic bandgap fibers: spectral properties, macrobending loss, and practical handling,” IEEE/OSA Journal of Lightwave Technology, vol. 22, pp. 11–15, Jan. 2004.

[36] Ziolkowski, R. W., "Incorporation of microscopic material models into FDTD approach for ultrafast optical propagation," IEEE Transactions on Antennas and Propagation, 375-391,(1997).

[35] Liang, T., Ziolkowski, R. W., "Dispersion effects on grating-assisted output couplers under ultrafast pulse excitations", Microwave and Opt. Tech. Lett., **17**, 17-23, (1998).

[37] Aleksandar D. Rakic, Aleksandra B. Djurisic, et. al., "Optical Properties of Metallic Films for Vertical - Cavity Optoelectronic Devices". 1998 Optical Society of America, August, Vol. 37, No. 22, Applied Optics, pp. 5271-5283.

[38] M. I. Markovic and A. D. Rakic, " Determination of reflection coefficients of laser light of wavelength $\lambda \in (0.22\mu m, 200\mu m)$ from the surface of aluminum using the Lorentz-Drude model", Appl. Opt. 29, 3479-3483 (1990).

[39] M. I. Markovic and A. D. Rakic, " Determination of optical properties of aluminum including electron reradiation in the Lorentz-Drude Model", Opt. Laser technol. 22, 394-398, (1990).